NASA
Technical
Paper
2417

April 1985

Flight-Measured Laminar Boundary-Layer Transition Phenomena Including Stability Theory Analysis

Clifford J. Obara
and Bruce J. Holmes

NASA

NASA Technical Paper 2417

1985

Flight-Measured Laminar Boundary-Layer Transition Phenomena Including Stability Theory Analysis

Clifford J. Obara
Kentron International, Inc.
Hampton, Virginia

Bruce J. Holmes
Langley Research Center
Hampton, Virginia

National Aeronautics and Space Administration

Scientific and Technical Information Branch

Summary

This report presents correlations of transition data from flight experiments with predictions using a boundary-layer computer code and a boundary-layer stability analysis method. The flight experiments were conducted on a single-engine turboprop aircraft fitted with a 92-in-chord natural laminar flow (NLF) glove. The boundary-layer transition measurement methods used included surface hot-film sensors and sublimating chemicals. Interpretation and analysis is given of hot-film signals for transition caused by pressure gradient and by flight through clouds. The results agree with previous measurements of transition due to laminar separation at low angles of attack. The flight conditions of this experiment include angles of attack from $-2°$ to $22°$, Reynolds numbers from 4×10^6 to 13×10^6, Mach numbers from 0.16 to 0.27, and glove section lift coefficients from 0.15 to 1.10. Transition occurred downstream of the minimum pressure point. Hot-film sensors provided a well-defined indication of laminar, laminar-separation, transitional, and turbulent boundary layers. There was good agreement between hot films and sublimating chemicals for detecting the transition front in flight. Theoretical calculations of the boundary-layer parameters provided close agreement between the predicted laminar-separation point and the measured transition location. Tollmien-Schlichting (T-S) wave growth n-factors between 15 and 17 were calculated at the predicted point of laminar separation. These results suggest that for many practical airplane cruise conditions, laminar separation (as opposed to T-S instability) is the major cause of transition in predominantly two-dimensional flows.

Introduction

The majority of early natural laminar flow (NLF) flight tests (ref. 1) relied on boundary-layer rakes that measured the velocity ratio u/u_e at given distances from the surface (typically greater than 0.10 in.). Characteristic shapes of u/u_e variations along the chord were used to indicate the location of transition for various Reynolds numbers. Very little data are available from those early tests to assist in distinguishing between Tollmien-Schlichting (T-S) instability and laminar separation as the cause of boundary-layer transition. Thus, the accuracy of transition prediction methods for the flight environment was limited by the accuracy of the measurement methods. In the mid-1940's, the use of sublimating chemicals (ref. 2) was introduced and provided a visual method for measuring the location of transition in flight. However, no information was available on the correlations between the locations of transition as measured by sublimating chemicals and by other methods. Surface hot films were introduced in the late 1950's (ref. 3) as a flight method for measuring transition. During the nearly 30-year hiatus in NLF flight research, which began in the early 1950's, very little detailed transition data in the flight environment were obtained.

This report presents the results of recent NLF flight experiments using sublimating chemicals and hot-film sensors for determining the location of boundary-layer transition. These methods have been refined or improved upon for the present flight experiments. The flight experiments were conducted on a single-engine turboprop aircraft fitted with a 92-in-chord NLF glove. Calculations using a boundary-layer analysis code and a boundary-layer stability analysis method are included. The objective of the paper is to provide some insight into and understanding of two-dimensional transition phenomena and transition measurement methods in the flight environment. Interpretation and analysis of hot-film signals are included for transition caused by pressure gradient and by flight through clouds.

Symbols

A	amplitude of boundary-layer disturbance
A_o	amplitude of boundary-layer disturbance at neutral stability
c	airfoil chord, ft
c_l	section lift coefficient
C_f	local skin-friction coefficient
C_p	pressure coefficient, $(p_l - p_\infty)/q_\infty$
h	pressure altitude, ft (mean sea level)
H	boundary-layer shape factor, δ^*/θ
M	Mach number
n	logarithmic exponent of T-S wave growth rates, $n = \ln(A/A_o)$
p	static pressure, psf
q	dynamic pressure, psf
R	Reynolds number based on free-stream conditions and local airfoil chord
R^*	hot-film probe resistance at temperature T
R'	unit Reynolds number based on free-stream conditions, ft^{-1}
R_o	hot-film probe resistance at temperature T_o
R_{δ^*}	Reynolds number based on boundary-layer displacement thickness and free-stream conditions

R_θ Reynolds number based on boundary-layer momentum thickness and free-stream conditions

T ambient temperature, °F

T_o reference temperature for hot-film probe resistance, °F

u local velocity in boundary layer, ft/sec

u_e boundary-layer edge velocity, ft/sec

V airspeed, knots

x longitudinal dimension, ft

y distance normal to surface, in.

z vertical dimension, ft

α angle of attack, deg

$\alpha^\star$ slope of change in resistance plotted against change in temperature for hot-film probe, ohms/°F

β frequency of T-S disturbance, Hz

δ boundary-layer thickness at height where $u = 0.995u_e$, in.

$\delta^\star$ boundary-layer displacement thickness, in.

θ boundary-layer momentum thickness, in.

ν kinematic viscosity, ft^2/sec

Subscripts:

i indicated

l local point on airfoil

max maximum

∞ free-stream conditions

Notation:

ips inches per second

FM frequency modulation

NLF natural laminar flow

T-S Tollmien-Schlichting

VCO voltage-controlled oscillator

Transition Phenomena

Osborne Reynolds' classical experiments demonstrated that under certain conditions, the flow in a tube changes (transitions) from laminar to turbulent. After a century of extending and expanding Reynolds' experiments, the mechanism of the laminar to turbulent transition process is still not completely understood. Many interdependent factors are involved in the stability of laminar flows and in the transition process. Large gains have been made in understanding the independent influences of these factors. These factors include pressure gradient, wing sweep, surface contamination and imperfections, free-stream turbulence, and noise. For most practical natural laminar flow (NLF) applications on modern aircraft, transition results from laminar separation (with turbulent reattachment), Tollmien-Schlichting (T-S) instability, crossflow instability, or contamination of the leading-edge attachment line. For the purpose of this paper, a brief synopsis is presented on each of these factors with a major emphasis placed on laminar separation and T-S instability.

Crossflow instability in the laminar boundary layer is a consequence of accelerating flow pressure gradients on a swept wing. Crossflow vorticity results from pressure gradients in the boundary layer normal to the direction of the external streamline. These crossflow vortices grow in strength in regions of accelerating flow and can amplify to cause transition.

Spanwise contamination of the leading-edge attachment line is found on wings with large leading-edge radii, large leading-edge sweep values, and large unit Reynolds numbers. Turbulence for contamination of the leading edge originates from such sources as supercritical leading-edge roughness elements or the turbulent fuselage boundary layer. This turbulence spreads spanwise along the attachment line and then chordwise to eliminate laminar flow on the surface.

The remaining factors that affect boundary-layer transition can occur on both swept and unswept wings. Transition can result from surface imperfections such as gaps, steps, or waviness. These imperfections, when large enough, can disturb the boundary layer and result in transition or a "trip" from laminar to turbulent flow at the imperfection. Practical illustrations of irregularities include skin joints for deicing boots, stall strips, vortex generators, and skin-lap or butt joints. Other causes of transition include ice accumulation, ice crystals in clouds, precipitation, and insect contamination. Engine noise frequencies found to be near the most unstable T-S wave frequencies in the boundary layer have also been effective in causing transition. (See ref. 4.)

Tollmien and Schlichting (ref. 5) obtained wave solutions to the Orr-Sommerfeld equation before such waves were observed experimentally (hence the name T-S instability). The existence of these disturbances was experimentally verified by Schubauer and Skramstad. (See ref. 6.) This disturbance originates near a wing leading edge as infinitesimally

small waves, which can amplify or damp as they move downstream. Should they amplify, experiment has shown that the waves will eventually break up into turbulent spots, which continue to spread and travel downstream and finally merge to form a fully turbulent region. Stability theory predicts that as the Reynolds number is increased up to the lower branch of the stability curve, disturbances of all frequencies are damped. This effect is shown in figure 1, where $\beta\nu/u_e^2$ is plotted against R_{δ^*} (ref. 7). For calculated values of $\beta\nu/u_e^2$ and R_{δ^*} that lie within the loop, designated the "neutral curve," the disturbance amplifies, but for values outside the loop, the disturbance is damped. The amplification of T-S waves is greatest in regions of adverse pressure gradient. The effect of a favorable pressure gradient (accelerating flow) is to retard the growth of T-S waves.

Laminar separation can occur in a region of adverse pressure gradient and cause transition. The separated boundary layer forms a free-shear layer, with transition occurring as the result of inflectional instability, followed by turbulent reattachment. At higher Reynolds numbers, the extent of this bubble is on the order of 1 percent of the chord and has little effect on the pressure distribution and forces acting on the airfoil. With an increase in incidence or a decrease in Reynolds number as it moves forward to the leading edge, the "short" bubble can form a "long" bubble. The extent of the long bubble can be from a few percent of the chord to full chord, and it will have a significant effect on the pressure distribution and the forces acting on the airfoil. At low angles of attack, Gault (ref. 8) measured transition due to the laminar separation far downstream from the leading edge on an NACA 66_3-018 airfoil section in a low-turbulence wind tunnel. In those tests, at a chord Reynolds number of 10×10^6, a transition length Reynolds number of 6.6×10^6 was measured at laminar separation.

Description of Test Airplane and Transition Measurement Methods

The Beechcraft T-34C, as shown in figure 2, is a single-engine turboprop aircraft with retractable gear. Geometric details are presented in figure 3 and table 1. The left wing of the airplane was fitted with a 92-in-chord, 3-ft span NLF glove. A NASA-designed NLF(1)-0215F airfoil section (ref. 9) was used for the glove. (See fig. 4 and table 2.) The performance envelope of the airplane offered a range of glove chord Reynolds numbers from 6.5 to 13×10^6.

Two techniques for determining boundary-layer transition were selected for the current flight experiments. The first method utilizes sublimating chemicals. (See refs. 2 and 10.) The technique involves coating the surface with a thin film of volatile chemical solid which, during exposure to free-stream airflow, rapidly sublimates in the turbulent boundary layer as a result of high shear stress and high mass transfer near the surface. (See fig. 5.) Transition is indicated by the fact that the chemical coating remains relatively unaffected in the laminar region because of lower shear and low mass transfer. Use of a chemical such as acenaphthene at ambient temperatures between 30°F and 90°F (at test altitude) offers the capability of flying to low test altitudes ($< 20\,000$ ft), stabilizing the sublimating chemical pattern at the test conditions, and returning to the ground with the chemical pattern unaffected by the off-condition portions of the flight required for climb to and descent from the test altitudes. The resulting range of flight times at the test conditions varies between 60 min at 30°F and 5 min at 90°F. Further details on the use of the techniques are given in reference 11.

Surface-mounted hot-film sensors were also used for measuring the location of boundary-layer transition. Each sensor consisted of a 0.004-in. by 0.035-in. nickel film deposited on a 0.002-in-thick polyimid film with a thin quartz coating. They are glued to the surface by using typical strain-gauge mounting techniques. (See fig. 6.) Shielded cables (RG-174/U) leading to the anemometer electronics are all soldered onto the copper leads. As installed on the T-34C glove, the sensor thicknesses ranged from 0.003 in. to 0.005 in. above the local airfoil surface. None of the sensors were large enough to cause local transition at the sensor for the highest test airspeeds, as verified by sublimating chemicals. (See fig. 6.) The six hot-film sensors were located at chord positions of 0, 5, 15, 20, 35, and 40 percent. (See fig. 4.) The figure illustrates the staggered position of the sensors to avoid contamination of a sensor from a neighboring upstream sensor.

Each of the hot films was operated in a constant (uncompensated) temperature mode. The anemometer electronics consists of the hot-film sensor as one side of a Wheatstone bridge circuit and includes an amplifier with programmable gain and filtering. A dc feedback loop maintains the sensor resistance at a constant level, which is equivalent to maintaining a constant temperature at the sensor surface. When the hot film is cooled as a result of an increase in air velocity or an increase in heat transfer rate, the resistance of the sensor changes by

$$R^\star = R_o + \alpha^\star(T - T_o)$$

where $R^\star$ is the sensor resistance at temperature T, R_o is the sensor resistance at temperature T_o,

and α^* is the slope of the resistance change plotted against temperature change in ohms/°F. The variation of the sensor resistance causes a voltage change in the Wheatstone bridge. This voltage change results in an increased current to the hot film. The fluctuating and mean values of heating voltage are recorded and observed in real time using an onboard battery-powered oscilloscope.

The ambient conditions to which the sensor is subjected determine the amount of energy necessary to maintain the sensor at a constant temperature. The heat loss of the sensor is dependent upon several factors, including conduction to the surface, local heat transfer through the boundary layer, atmospheric pressure and temperature, velocity of the airflow, and moisture.

The melting temperature of the sensor material limits the upper temperature at which the sensor can be operated. However, the optimum sensitivity is obtained by using a high overheat ratio R/R_o. The highest allowable overheat ratio for the T-34C sensors was 1.60; above this value the sensor would melt. For the T-34C glove experiments, the overheat ratio was set to 1.46 at a nominal ambient temperature of 68°F. Because of changes in local ambient temperature, the in-flight overheat ratios ranged from 1.37 to 1.56.

Figure 7 is a block diagram of the hot-film flight instrumentation system. All the data were recorded by frequency modulation (FM) on magnetic tape at 15 ips. The data were recorded over two frequency ranges; dc to 200 Hz (mean hot-film voltage) was recorded using constant bandwidth FM voltage-controlled oscillators (VCO) and dc to 10 kHz (fluctuating hot-film voltage) was recorded using wideband VCO's.

Figure 8 is an idealized description of the fluctuating or high-frequency signals from the hot-film sensors. Within the laminar region, where there is a slow, steady heat transfer rate, the sensor requires less voltage input to keep the temperature constant; hence, there is a low amplitude signal. The low level of signal amplitude in the illustration indicates the presence of noise in the instrumentation system. A noise-free laminar signal would have zero amplitude. In the turbulent region, where there are large velocity changes with the rapid fluctuating heat transfer rates, a larger voltage change is required and results in signals of greater amplitude.

The noise that is found in the data from the present hot-film system has a level of 4 mV peak to peak or 2.8 mV rms. This noise gets into the data through the power supplies in the anemometer signal conditioner. The signal conditioner is powered by a 115 V 400 cycle power supply. The 400 cycles pass through other power supplies in the signal conditioner and appear in the data. Probe cable length, cable type, grounding techniques, and bridge balance can also affect the noise level. By fine tuning each of these items, a minimum noise level and greater sensitivity of the system can be obtained. The increased sensitivity simplifies interpretation of hot-film response to transition and can provide data for measurement of T-S frequencies.

Analytical Methods

Calculations were made of boundary-layer characteristics using two computer codes. The two codes provided predictions of boundary-layer velocity profiles for an infinite yawed wing and calculated two-dimensional instability growth in the laminar-flow region. Input to the first program by Kaups and Cebeci (hereinafter referred to as the Cebeci code, ref. 12) consists of the measured pressure distribution along with free-stream flow parameters. Output consists of boundary-layer velocity profiles and the common integral boundary-layer parameters. The Cebeci code utilizes a box finite-difference method to solve the governing three-dimensional laminar boundary-layer equations in polar form. The program predicts the location of laminar separation when the laminar boundary-layer equations no longer converge.

A two-dimensional linear stability analysis of the laminar velocity profiles was calculated by the SALLY (Stability Analysis which is Local, Linear, and Incompressible) program. (See ref. 13.) The code utilizes Chebyshev polynomials to approximate solutions to the Orr-Sommerfeld stability equation by giving the amplification of a specified-frequency T-S wave for incompressible flows. The velocity profiles (from the Cebeci code), the Reynolds number based on displacement thickness, the desired frequencies of disturbance, and the ranges of corresponding wavelengths are required for input. Output consists of the natural logarithm of the amplitude ratio of the T-S waves, beginning at the initial point of instability and continuing to the point of predicted laminar separation. For this study, the SALLY code was run to obtain only the two-dimensional linear T-S growth, although it has the capability to calculate crossflow instability growth as well.

In the past, linear stability theory has been calibrated by calculating the predicted amplitude ratio e^n at flight- and wind-tunnel-measured transition locations. All these calibration calculations have assumed that transition was caused by T-S amplification to transition (except for the swept-wing calibrations, which assume an influence of crossflow instability). For the boundary-layer T-S disturbance

and amplification process, linear growth can dominate the transition process. (See ref. 14.) Past n-factor analyses for flight data have produced values of n from 15 to > 20 on airfoils. (See refs. 11, 15, and 16.) For these past flight data, transition occurred downstream of the point of minimum pressure and could have been initiated by laminar separation. Thus, these n-factors may have been calculated for laminar-separation locations rather than for T-S transition.

Results and Discussion

The flight tests were conducted over a range of angles of attack from $-2°$ to $22°$, Reynolds numbers from 4×10^6 to 13×10^6, Mach numbers from 0.16 to 0.27, and glove section lift coefficients from 0.15 to 1.10. Static-pressure measurements were made with internal, flush static ports. In addition to measurements at discrete test conditions, acceleration-deceleration tests were conducted in order to sweep through a continuous range of angle of attack and hence, a range of transition locations.

Figure 9 presents the measured pressure distributions for three sets of flight conditions. In all three cases, a bump appeared in the pressure distribution for the upper surface at a distance of 8 percent of the chord from the leading edge. This was due to a 2.5-in. wavelength, 0.010-in. double amplitude wave in the airfoil surface at an internal support structure joint. Also included in figure 9 are the predicted pressure distributions using the two-dimensional airfoil code developed by Eppler and Somers. (See ref. 17.) The differences for the upper surface appear as a lower pressure gradient in the forward region for the predicted values, followed by larger values of absolute pressure coefficient in the aft region. These differences between the measured pressure distribution and the two-dimensional theory indicate the effect of the finite span (3 ft) of the glove on the potential flow. The three measured pressure distributions are contained in table 3 and represent the test conditions for the analysis of subsequent transition locations.

Sublimating chemicals were used to determine the boundary-layer transition location on the glove at the test conditions presented in figure 9(a). Transition occurred at 44-percent chord along the midspan. (See fig. 10.) The wave in the nose region had no effect on transition location. A single insect strike caused a turbulent wedge to form on the inside half of the glove.

An analysis was conducted to determine the T-S amplification ratio for the two-dimensional laminar boundary-layer disturbances at test conditions corresponding to the pressure distributions in figures 9(a) and 9(b). Selected velocity profiles computed by the Cebeci code are shown in figures 11(a) and 11(b). These profiles correspond to the test conditions and upper-surface pressure distributions of figures 9(a) and 9(b), respectively. Also, the calculated boundary-layer parameters are contained in table 4. As indicated in the table, at transition, R_θ was as large as 1553 for the case with $R = 12.6 \times 10^6$. Figure 12 shows the amplification of various T-S frequencies for the upper surface of the glove. The analysis was run using the measured upper-surface pressure distribution of figure 9(a), the calculated velocity profiles of figure 11(a), a Reynolds number of 12.6×10^6, and a Mach number of 0.27. The transition location marked in the figure is the laminar-separation point as predicted by the Cebeci code. However, the observed transition location in flight is in close proximity to this point. The analysis resulted in a maximum amplification of $n = 15$ at 45-percent chord. The 2250-Hz frequency experiences the greatest amplification; the theory assumes this frequency to have primary responsibility for the transition process.

Figure 13 shows another analysis of the amplification of T-S disturbances on the upper surface of the glove. The test conditions appear in figures 9(b) and 11(b). The transition location was measured using the hot-film sensors and was taken to be the position of the fully developed turbulent boundary layer (discussed in detail in the section "Level Flight Acceleration"). Correlations (by simultaneous testing) in flight show that the sublimating-chemical indication of transition agrees with the hot-film indication of completion of the transition region at the fully developed turbulent boundary layer. Maximum amplification at the transition location of 40-percent chord was $n \approx 17$ at a frequency of 2000 Hz. Both of these stability analyses show that for the flight environment n-factors equal to or greater than 15 occur. This result is consistent with other published stability analyses of flight transition data. (See refs. 11, 15, and 16.) All these past analyses have been conducted assuming that transition occurred due to the growth of T-S instability. In two-dimensional flows, flight-measured transition has nearly always occurred downstream of the point of minimum pressure (e.g., see refs. 18 and 19). If transition in those flight data were caused by laminar separation, then the resulting values of n are not useful as a criterion for predicting transition of any kind. However, use of an n-factor of 15 will provide a conservative estimate for the design of favorable pressure gradients required for transition to occur near the point of minimum pressure for the range of unit Reynolds numbers of this investigation ($0.5 \times 10^6 < R' < 1.7 \times 10^6$ ft^{-1}).

Level Flight Acceleration

The data presented in this section illustrate the character of hot-film transition signals for transition caused by pressure gradient changes during a level-flight acceleration (continuously decreasing angle of attack). Flight conditions (fig. 14(a)) and hot-film signal characteristics (figs. 14(b) and 14(c)) are presented for an acceleration from 80 knots to 145 knots. The sensor at $x/c = 0.40$ was amplified electronically prior to data recording; thus it has an overall larger amplitude signal. At the highest angle of attack (lowest airspeed), transition is located forward of the sensor at 15-percent chord and aft of the sensors at 0- and 5-percent chord. The sensors at 0- and 5-percent chord remained laminar throughout the acceleration. The laminar signals show the 4-mV noise level discussed previously. Several features of transition may be observed in figures 14(b) and 14(c). The pressure distributions corresponding to the occurrence of transition at the $x/c = 0.40$ and 0.35 sensors were presented in figures 9(b) and 9(c), respectively. Also, transition occurs downstream of the peak (miminum) pressure.

The transition region can exhibit three phases. As transition moves across a fixed chord location, the first phase can consist of intermittent turbulent bursts in the laminar boundary layer. This intermittency increases as the turbulent bursts become longer in duration until the beginning of the second phase. An example of this first phase is seen most clearly in figure 14(b) for the sensor at $x/c = 0.40$ (90 to 120 sec). For sensors at $x/c = 0.15$, 0.20, and 0.35, this intermittency phase appears to have been almost nonexistent. The second phase consists of very large amplitude, high-frequency fluctuations superimposed on a lower frequency (about 3 to 6 sec per cycle) large-amplitude oscillation; for example, note the sensor signals at $x/c = 0.15$, 0.35, and 0.40 (fig. 14(b)) in the transition regions. In the third and final phase of the transition region, high-frequency, nearly constant amplitude fluctuations mark the beginning of the fully turbulent boundary layer; for example, see the 8-sec time position for sensors at $x/c = 0.15$ and 0.20, and the 52- and 62-sec positions for sensors at $x/c = 0.35$ and 0.40, respectively. The middle (second) phase appears similar in nature to the signal characteristics reported by Lobel (ref. 20) for laminar-separation bubbles as measured with the same kind of surface hot-film sensors.

The hot-film steady-state output shown in figure 14(c) also exhibits these three phases. At $x/c = 0$ and 0.05, the sensors record laminar flow throughout the acceleration maneuver. The remaining steady-state sensor signals illustrate the changes from laminar to turbulent. The first phase, with intermittency in the laminar boundary layer, appears at $x/c = 0.40$ between about 90 and 120 sec. The second phase, which appeared in the high-frequency signal as large-amplitude low-frequency oscillations, appears in a similar fashion in the steady-state signals. The sensors at $x/c = 0.15$, 0.35, and 0.40 illustrate these oscillations most clearly. The third phase, completing the transition region, is less sharply defined in the steady-state signals than in the high-frequency signals. It is generally characterized by an overall increase in the steady-state signal level from the laminar condition; for the transition data shown here, a rise of about 0.2 V (out of full scale of 5.0 V) occurs in the turbulent boundary layer. Although not as useful as calculated values of intermittency, the steady-state signals are useful in interpreting the time-averaged state of the transition process from laminar to turbulent flow.

The transition signals shown indicate that the transition region can be well-defined for the two-dimensional flows studied. For purposes of transition measurement in flight research, the downstream end of the transition region (fully developed turbulent flow) is the most clearly delineated point in the transition region. This point also corresponds well to the transition front indicated by sublimating chemicals. Further research is warranted to study the nature of transition at these Reynolds numbers and the interpretation of laminar-separation-bubble transition signals in hot films.

Flight Through Clouds

Two sets of hot-film data are presented for flight through clouds. For one set, extensive loss of laminar flow occurred, and for the other set extensive loss of laminar flow did not occur. These data illustrate the different characteristics of the hot-film transition signals for transition caused by flight in clouds compared with transition caused by pressure gradient (e.g., fig. 14). Visual cues were used to record cloud entry and exit; an event signal was recorded on the temperature channel by manually pressing an event button at the cloud entry and exit times. Constant angle of attack was desired during the cloud encounters; however, the large-scale atmospheric motion which existed within the clouds caused changes in angle of attack and airspeed which must be carefully accounted for when interpreting the hot-film transition signals.

Flight conditions (fig. 15(a)) and hot-film signal characteristics (figs. 15(b) and 15(c)) are presented for flight through two clouds, during which extensive loss of laminar flow was indicated by the hot films. These cloud entries occurred at speeds of 150 and

134 knots at pressure altitudes of 5500 and 6000 ft, a temperature of about 62°F, and a unit Reynolds number of 1.5×10^6 ft^{-1}. During flight through these clouds, a mist deposited on the windscreen of the airplane and presumably deposited on the glove leading edge. No downstream spreading of this mist was observed, and the mist totally evaporated from the windscreen a few seconds after cloud exit. The large spikes or jumps in the temperature plot are created by the event button discussed previously.

The features of transition as indicated by high-frequency and steady-state hot-film response to transition in clouds differ from the pressure-gradient-induced transition mainly by the lack of any large-amplitude, low-frequency oscillations discussed in the "second phase" of the transition region for level-flight accelerations. The sensor at $x/c = 0$ exhibits a very large increase in amplitude of the high-frequency signal (fig. 15(b)), a small increase in the steady-state signal (fig. 15(c)) upon cloud entry, and a return to laminar signals upon cloud exit. Whether these signal changes are due to turbulent boundary layer or due to impingement on the sensor by the mist particles is not clear. Since a finite time after cloud exit was required for mist evaporation from the surface, and since this signal returns to laminar soon after cloud exit, it is clear that the wetting of the sensor alone is not responsible for the signals shown. The sensor at $x/c = 0.05$ appears unaffected by the cloud particles. Since the hot films are not aligned physically in the chordwise direction behind the sensor at $x/c = 0$, it is probable that the effect of the mist deposit on the boundary layer is not uniform in the spanwise direction. The fact that the sensors are staggered spanwise may also explain uncorrelated transition onset and laminar recovery times for the downstream sensors at $x/c = 0.15$, 0.20, 0.35, and 0.40. At $x/c = 0.15$, 0.20, 0.35, and 0.40, the boundary-layer transitions briefly to turbulent, then recovers to laminar. These sensors exhibit a sharp downward transient signal as laminar flow is recovered. In the steady-state hot-film response, these sharp transients appear as about a 0.2-V drop in the signal (which is the same rise as for transition caused by pressure gradient).

In figures 16(a), 16(b), and 16(c), a cloud encounter is illustrated which does not cause extensive loss of laminar flow. During this cloud encounter, no mist deposit was observed on the windscreen. The steady-state signals (fig. 16(c)) show that none of the sensors indicate turbulent boundary-layer conditions during the cloud encounter, although the sensor at $x/c = 0.40$ does exhibit some intermittency. The turbulent flow for this sensor after exiting the cloud, between 35 and 50 sec, was caused by the pressure gradient at the increased angle of attack due to free-stream turbulence outside the clouds. These measurements suggest that unless some form of surface contamination occurs (such as mist deposit, rain, or ice), laminar flow is not lost in clouds for the conditions of this experiment.

Further studies on the effects of flight through clouds on transition should be conducted if possible with hot-film sensors aligned in the streamwise direction. In order to distinguish the effects on transition of cloud particles from pressure gradient, a careful correlation should be made between angle of attack and airfoil pressure distribution (and Mach number where significant). In addition, electronic sensing of cloud entry and exit is advised over visual marking of these events.

Concluding Remarks

Natural laminar flow flight experiments were conducted on an instrumented airfoil glove installed on the Beechcraft T-34C aircraft. Airfoil pressure distributions were measured, and both sublimating chemicals and hot-film sensors were used to measure the boundary-layer transition location. Analysis was conducted of the laminar boundary-layer stability using linear stability theory. Interpretation and analysis was given of hot-film signals for transition caused by pressure gradient and by flight through clouds. The following specific conclusions are drawn based on the results:

1. For the flight conditions of this experiment, namely, angles of attack from $-2°$ to $22°$, chord Reynolds numbers from 4×10^6 to 13×10^6, Mach numbers from 0.16 to 0.27, and glove section lift coefficients from 0.15 to 1.10, transition occurred downstream of the minimum pressure point.

2. Theoretical calculations of the boundary-layer parameters provided Tollmien-Schlichting (T-S) wave growth n-factors between 15 and 17 for the test points studied. These factors were obtained at the predicted point of laminar separation.

3. Hot-film sensors provided a well-defined indication of laminar, transitional, and turbulent boundary-layer states. Laminar-separation bubbles were detected with the sensors. Both high-frequency and steady-state hot-film response signals were useful for transition interpretation. There was good agreement between hot-film sensors and sublimating chemicals for detecting the transition front in flight. These measurements also agreed closely with the predicted laminar-separation point.

4. For the conditions of the present flight experiments, cloud particles which do not form a mist deposit on the wing do not cause extensive loss of lami-

nar flow. With a mist deposit on the wing, extensive loss of laminar flow occurs at the test condition where free-stream unit Reynolds number is 1.5×10^6 ft^{-1}.

5. It can be inferred that laminar-separation bubbles were the dominating cause of boundary-layer transition, rather than the two-dimensional T-S instability. The results provide increased confidence that for many practical airplane free-stream conditions, laminar separation is the major cause of transition in predominantly two-dimensional flows. For these conditions, the use of n-factors for predicting transition is not appropriate, except for designing conservative pressure gradients required for satisfactory T-S stability in the flight environment.

NASA Langley Research Center
Hampton, VA 23665
December 18, 1984

References

1. Holmes, Bruce J.; Obara, Clifford J.; and Yip, Long P.: *Natural Laminar Flow Experiments on Modern Airplane Surfaces.* NASA TP-2256, 1984.
2. Pringle, G. E.; and Main-Smith, J. D.: *Boundary-Layer Transition Indicated by Sublimation.* Tech. Note No. Aero. 1652, British R.A.E., June 1945.
3. Banner, Richard D.; McTigue, John G.; and Petty, Gilbert, Jr.: *Boundary-Layer-Transition Measurements in Full-Scale Flight.* NACA RM H58E28, 1958.
4. Carmichael, Bruce H.: *Summary of Past Experience in Natural Laminar Flow and Experimental Program for Resilient Leading Edge.* NASA CR-152276, 1979.
5. Schlichting, Hermann (J. Kestin, transl.): *Boundary Layer Theory.* McGraw-Hill Book Co., Inc., 1979.
6. Schubauer, G. B.; and Skramstad, H. K.: *Laminar-Boundary-Layer Oscillations and Transition on a Flat Plate.* NACA Rep. 909, 1948.
7. Kuethe, Arnold M.; and Chow, Chuen-Yen: *Foundations of Aerodynamics: Bases of Aerodynamic Design,* Third ed. John Wiley & Sons, c.1976.
8. Gault, Donald E.: *An Experimental Investigation of Regions of Separated Laminar Flow.* NACA TN 3505, 1955.
9. Somers, Dan M.: *Design and Experimental Results for a Flapped Natural-Laminar-Flow Airfoil for General Aviation Applications.* NASA TP-1865, 1981.
10. Main-Smith, J. D.: *Chemical Solids as Diffusible Coating Films for Visual Indications of Boundary-Layer Transition in Air and Water.* R. & M. No. 2755, British A.R.C., 1950.
11. Holmes, Bruce J.; Obara, Clifford J.; Gregorek, Gerald M.; Hoffman, Michael J.; and Frueler, Rick J.: Flight Investigation of Natural Laminar Flow on the Bellanca Skyrocket II. SAE Paper 830717, Apr. 1983.
12. Kaups, Kalle; and Cebeci, Tuncer: Compressible Laminar Boundary Layers With Suction on Swept and Tapered Wings. *J. Aircr.*, vol. 14, no. 7, July 1977, pp. 661-667.
13. Srokowski, Andrew J.; and Orszag, Steven A.: Mass Flow Requirements for LFC Wing Design. AIAA Paper 77-1222, Aug. 1977.
14. Hefner, Jerry N.; and Bushnell, Dennis M.: *Status of Linear Boundary-Layer Stability Theory and the e^n Method, With Emphasis on Swept-Wing Applications.* NASA TP-1645, 1980.
15. Viken, Jeffrey K.: Aerodynamic Design Considerations and Theoretical Results for a High Reynolds Number Natural Laminar Flow Airfoil. M.S. Thesis, George Washington Univ., Jan. 1983.
16. Runyan, L. James; and George-Falvy, Dezso: Amplification Factors at Transition on an Unswept Wing in Free Flight and on a Swept Wing in Wind Tunnel. AIAA Paper 79-0267, Jan. 1979.
17. Eppler, Richard; and Somers, Dan M.: *A Computer Program for the Design and Analysis of Low-Speed Airfoils.* NASA TM-80210, 1980.
18. Goett, Harry J.; and Bicknell, Joseph: *Comparison of Profile-Drag and Boundary-Layer Measurements Obtained in Flight and in the Full-Scale Wind Tunnel.* NACA TN 693, 1939.
19. Tani, Itiro: *On the Design of Airfoils in Which the Transition of the Boundary Layer is Delayed.* NACA TM 1351, 1952.
20. Lobel, R.: *Identification of Flow Type Using Heated Thin Films.* OUEL Rep. No. 1238/78, Univ. of Oxford, Apr. 1978.

TABLE 1. DESCRIPTION OF BEECHCRAFT T-34C AND NLF GLOVE

Gross weight, lb	4300
Wing:	
Airfoil, root	NACA 23016.5 (modified)
Airfoil, tip	NACA 23012
Area, ft^2	179.6
Span, ft	33.325
Aspect ratio	6.22
Taper ratio	0.414
Root chord, ft	8.358
Tip chord, ft	3.458
Mean aerodynamic chord, ft	6.247
Incidence (root), deg	4.0
Incidence (tip), deg	1.0
Dihedral, deg	7.0
Powerplant:	
Manufacturer	Pratt & Whitney Aircraft of Canada
Model	PT6A-25
Maximum continuous power, shp	550
Propeller (constant speed):	
Manufacturer	Hartzell
Model	T10173-11R
Number of blades	3
Diameter, ft	7.5
Revolutions per minute, max	2200
Glove:	
Airfoil	NLF(1)-0215F
Area, ft^2	23.0
Span, ft	3.0
Chord, ft	7.667

TABLE 2. T-34C NLF(1)-0215F AIRFOIL GLOVE COORDINATES

(a) Theoretical coordinates from reference 9

Upper surface	
x/c	z/c
0.00000	−0.00006
.00240	.00917
.00909	.01947
.02004	.03027
.03527	.04120
.05469	.05201
.07816	.06250
.10546	.07247
.13635	.08175
.17050	.09019
.20758	.09761
.24720	.10389
.28894	.10887
.33237	.11240
.37702	.11428
.42253	.11427
.46864	.11219
.51524	.10784
.56247	.10147
.61010	.09373
.65752	.08513
.70408	.07603
.74914	.06673
.79206	.05746
.83222	.04844
.86902	.03983
.90193	.03175
.93044	.02428
.95409	.01737
.97285	.01082
.98710	.00507
.99658	.00126
1.00000	.00000

Lower surface	
x/c	z/c
0.00000	−0.00006
.00245	−.00704
.01099	−.01211
.02592	−.01656
.04653	−.02052
.07242	−.02399
.10324	−.02699
.13854	−.02954
.17788	−.03166
.22073	−.03334
.26654	−.03456
.31473	−.03531
.36468	−.03554
.41576	−.03519
.46731	−.03415
.51867	−.03225
.56920	−.02925
.61825	−.02441
.66662	−.01663
.71614	−.00705
.76645	.00167
.81565	.00804
.86198	.01155
.90359	.01198
.93862	.00990
.96588	.00655
.98504	.00323
.99630	.00086
1.00000	.00000

TABLE 2. Concluded

(b) Actual airfoil coordinates, $c = 92$ in.

Upper surface	
x/c	z/c
0.00000	0.00000
.00241	.01058
.00910	.02053
.02008	.03119
.03534	.04201
.05479	.05306
.07832	.06432
.10567	.07404
.13662	.08274
.17084	.09105
.20799	.09871
.24769	.10532
.28951	.11047
.33303	.11396
.37777	.11558
.42337	.11533
.46957	.11298
.51626	.10861
.56358	.10259
.61131	.09504
.65883	.08617
.70547	.07691
.75063	.06732
.79364	.05792
.83387	.04906
.87074	.04069
.90372	.03266
.93228	.02496
.95598	.01794
.97478	.01175
.98907	.00659
.99855	.00304
1.00000	.00262

Lower surface	
x/c	z/c
0.00000	0.00000
.00245	−.00703
.01101	−.01244
.02597	−.01636
.04662	−.02014
.07257	−.02388
.10344	−.02737
.13882	−.03027
.17823	−.03239
.22116	−.03381
.26707	−.03466
.31535	−.03519
.36540	−.03502
.41658	−.03438
.46823	−.03361
.51969	−.03228
.57031	−.02948
.61966	−.02398
.66793	−.01627
.71755	−.00735
.76795	.00098
.81725	.00793
.86367	.01104
.90536	.01085
.94046	.00828
.96777	.00507
.98698	.00211
.99826	.00012
1.00000	.00001

TABLE 3. TABULATED MEASURED PRESSURE DATA

Pressure orifice location, x/c	C_p for $c_l = 0.35$	C_p for $c_l = 0.54$	C_p for $c_l = 0.69$
Upper surface			
0.00240	0.876	0.573	0.355
.00571	.659	.270	.054
.01054	.402	−.019	−.251
.01531	.215	−.210	−.428
.02042	.091	−.320	−.530
.02543	−.012	−.419	−.572
.03073	−.102	−.481	−.639
.04038	−.202	−.562	−.690
.05033	−.286	−.625	−.724
.06028	−.379	−.704	−.791
.07524	−.527	−.839	−.909
.10043	−.621	−.888	−.935
.15095	−.673	−.881	−.892
.20057	−.751	−.930	−.909
.25065	−.817	−.954	−.916
.30072	−.840	−.973	−.874
.40057	−.798	−.833	−.757
.50090	−.653	−.684	−.571
.60085	−.442	−.482	−.336
.70050	−.280	−.297	−.143
.80240	−.161	−.160	−.008
.90176	−.120	−.105	−.044
Lower surface			
0.00000	0.943	1.068	1.070
.00438	−.293	.417	.941
.00998	−.379	.189	.698
.01498	−.275	.195	.641
.01998	−.227	.178	.599
.02489	−.210	.153	.548
.03002	−.185	.153	.526
.04010	−.151	.141	.493
.05010	−.154	.110	.445
.05995	−.168	.091	.403
.07485	−.164	.049	.361
.09988	−.217	−.013	.286
.14999	−.158	.006	.269
.20012	−.154	−.019	.243
.25007	−.210	−.142	.126
.29990	−.251	−.136	.109
.40006	−.241	−.136	.086
.49993	−.275	−.179	.018
.60019	−.355	−.290	−.100
.69940	−.044	.012	.178
.80001	.195	.252	.406
.89983	.285	.333	.490

TABLE 4. T-34C NLF GLOVE UPPER-SURFACE BOUNDARY-LAYER PARAMETERS

[Calculated from ref. 12]

$c_l = 0.35$; $R = 12.6 \times 10^6$; $V_i = 178.0$ knots; $M = 0.27$						
x/c	δ^*, in.	R_{δ^*}	θ, in.	R_θ	H	C_f
0.000	0.001785	245	0.000702	96	2.54	4.441
.003	.004628	635	.001831	251	2.53	1.780
.007	.004894	672	.001932	265	2.54	1.660
.020	.006330	869	.002438	335	2.59	1.284
.060	.009660	1326	.003717	510	2.61	.868
.100	.012328	1692	.004646	638	2.66	.675
.200	.017204	2362	.006495	892	2.65	.509
.300	.021252	2918	.007940	1090	2.68	.415
.350	.023828	3271	.008804	1209	2.71	.371
.400	.027048	3713	.009844	1351	2.75	.323
.425	.029256	4016	.010488	1440	2.80	.289
.450	.032476	4458	.011316	1553	2.87	.253
$c_l = 0.54$; $R = 8.6 \times 10^6$; $V_i = 146.0$ knots; $M = 0.22$						
0.000	0.001981	185	0.000780	73	2.54	7.223
.003	.004442	415	.001745	163	2.55	3.298
.007	.005323	498	.002073	194	2.57	2.730
.020	.007480	699	.002873	269	2.60	1.947
.060	.011685	1092	.004488	420	2.60	1.291
.100	.015165	1418	.005686	532	2.67	.978
.200	.021124	1975	.008011	749	2.64	.741
.300	.025969	2428	.009762	913	2.66	.614
.325	.028151	2631	.010416	974	2.70	.552
.350	.031132	2910	.011275	1054	2.76	.489
.375	.035041	3276	.012334	1153	2.84	.415
.400	.040114	3750	.013605	1272	2.95	.346

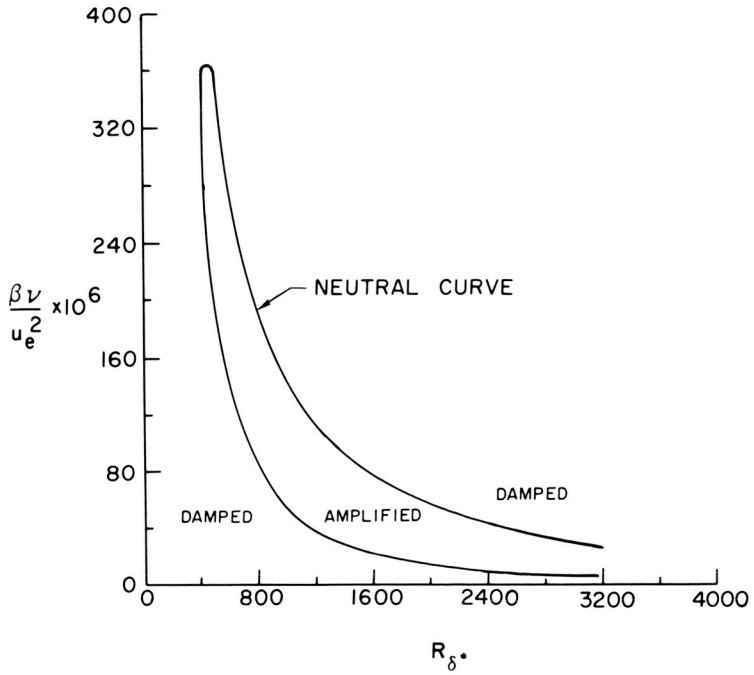

Figure 1. Laminar boundary-layer stability on a flat plate (ref. 7).

L-81-4814

Figure 2. Beechcraft T-34C fitted with NLF glove.

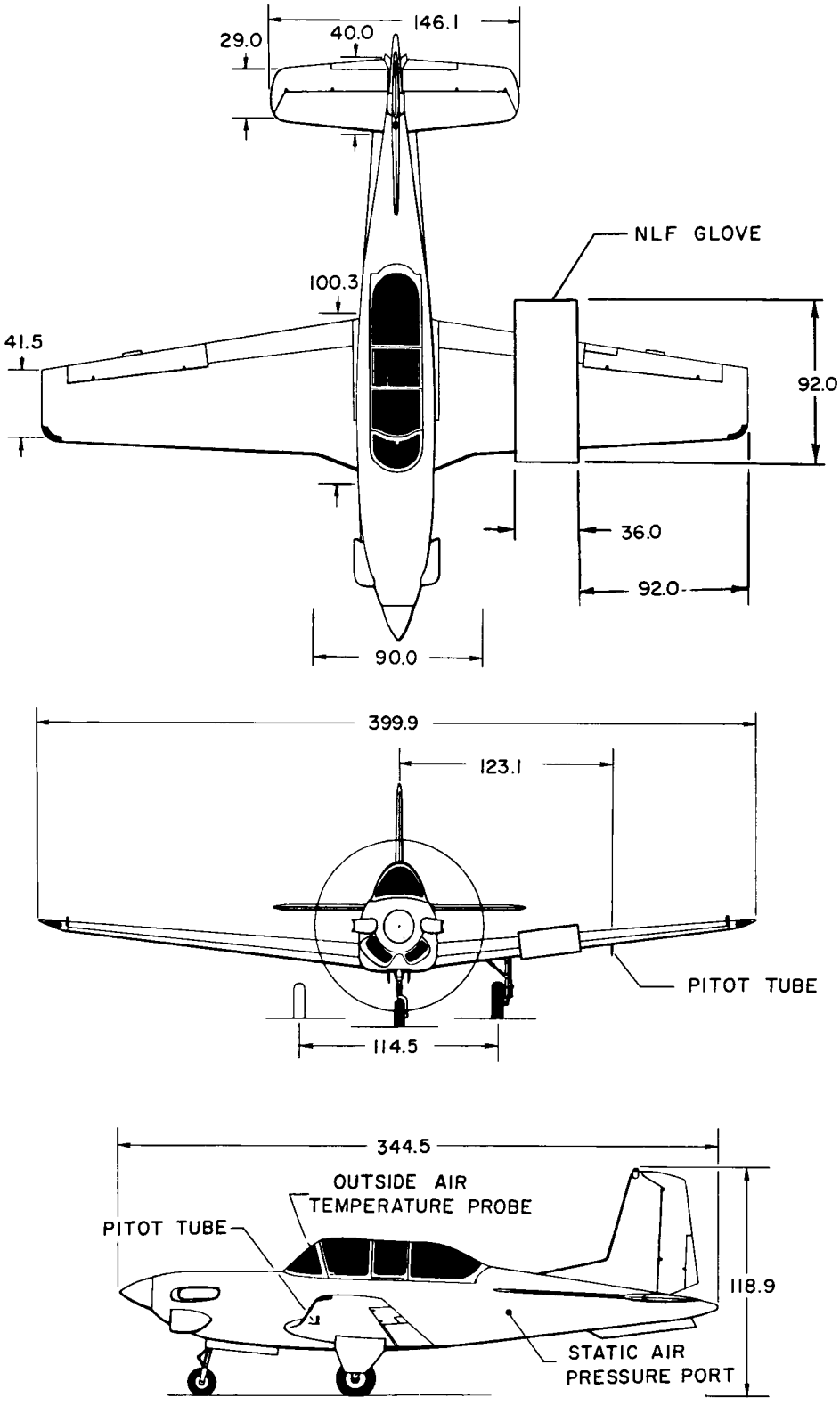

Figure 3. Three-view of Beechcraft T-34C. (All dimensions are in inches.)

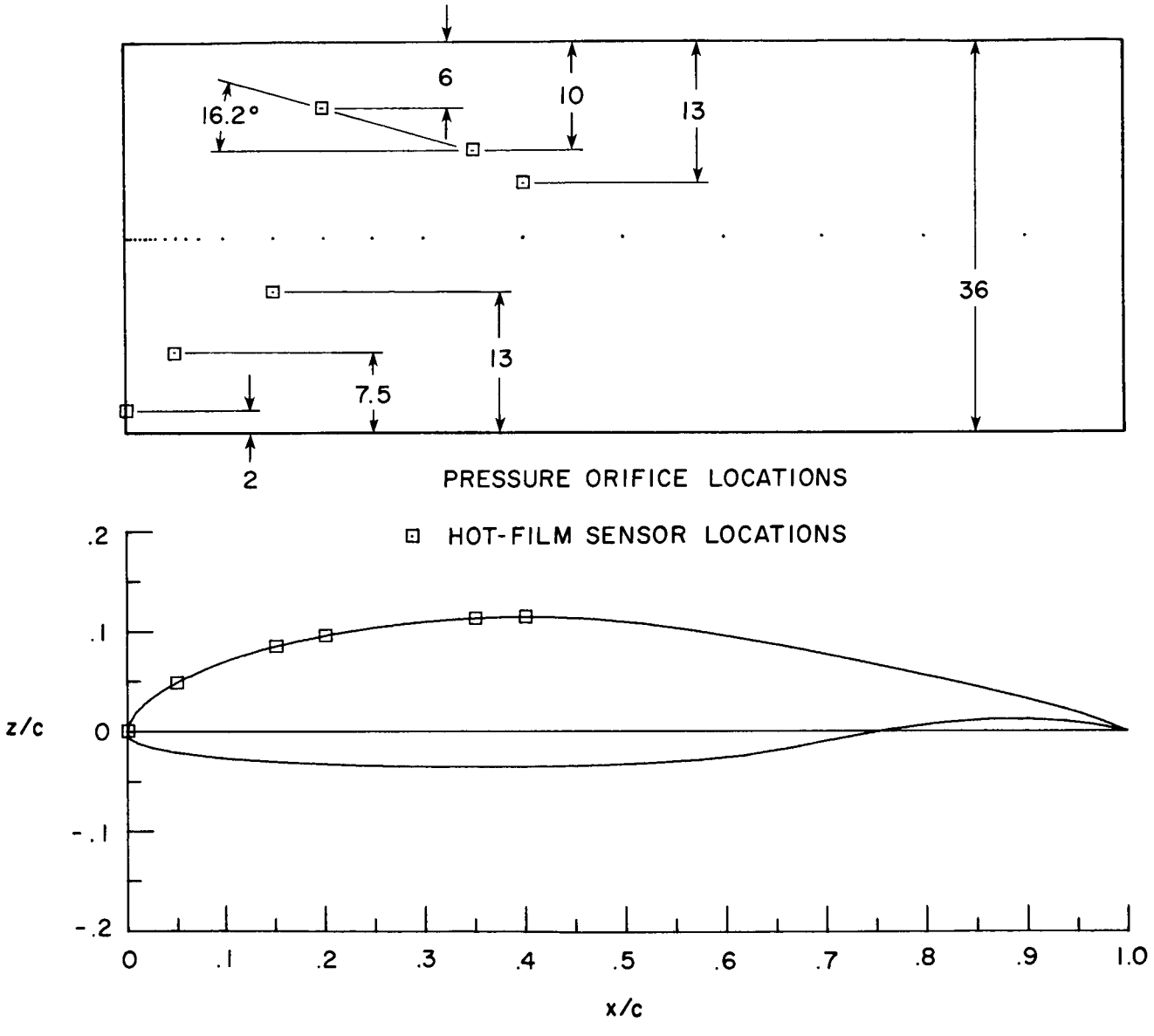

Figure 4. NLF(1)-0215F airfoil section as used on NLF glove, including hot-film sensor locations. (All linear dimensions are in inches.)

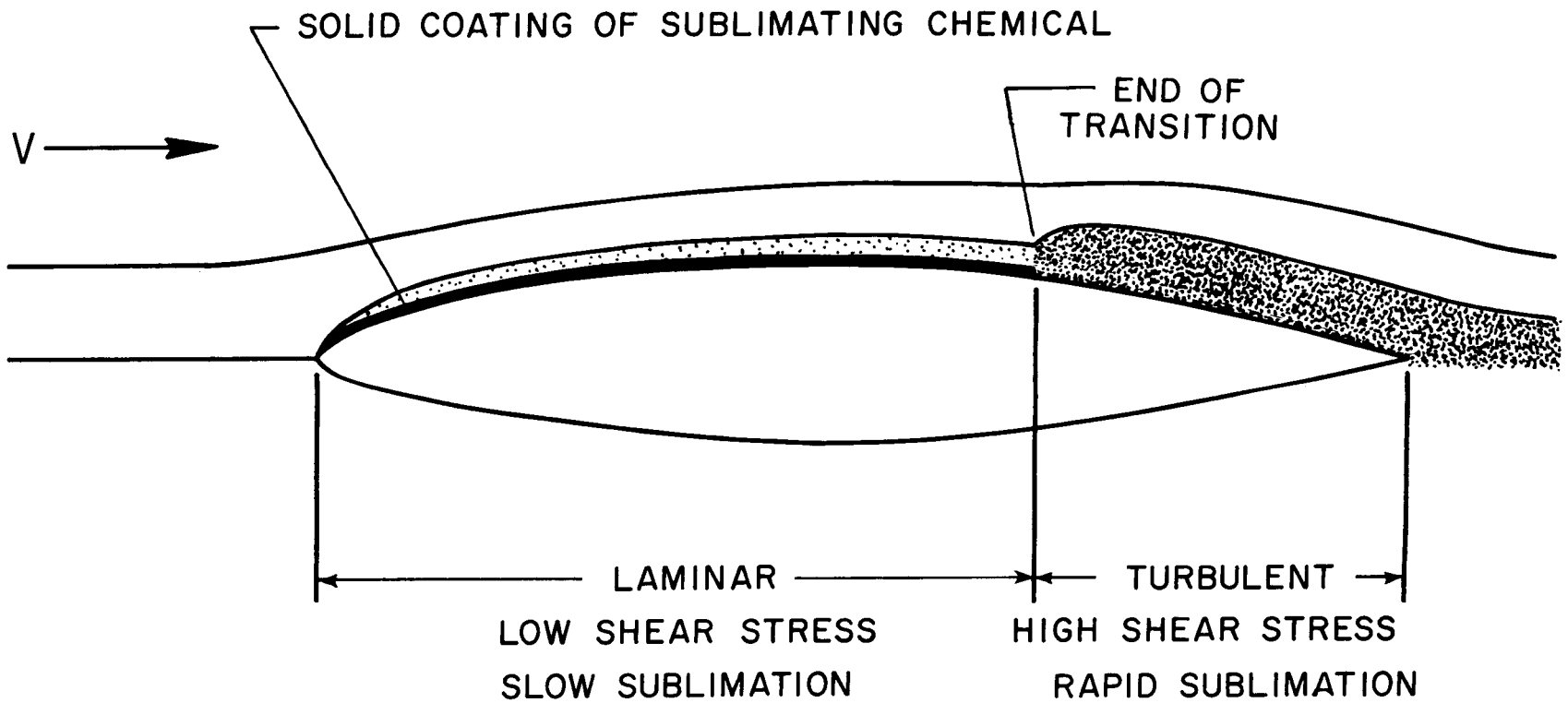

Figure 5. Visual description of how sublimating chemicals indicate boundary-layer transition.

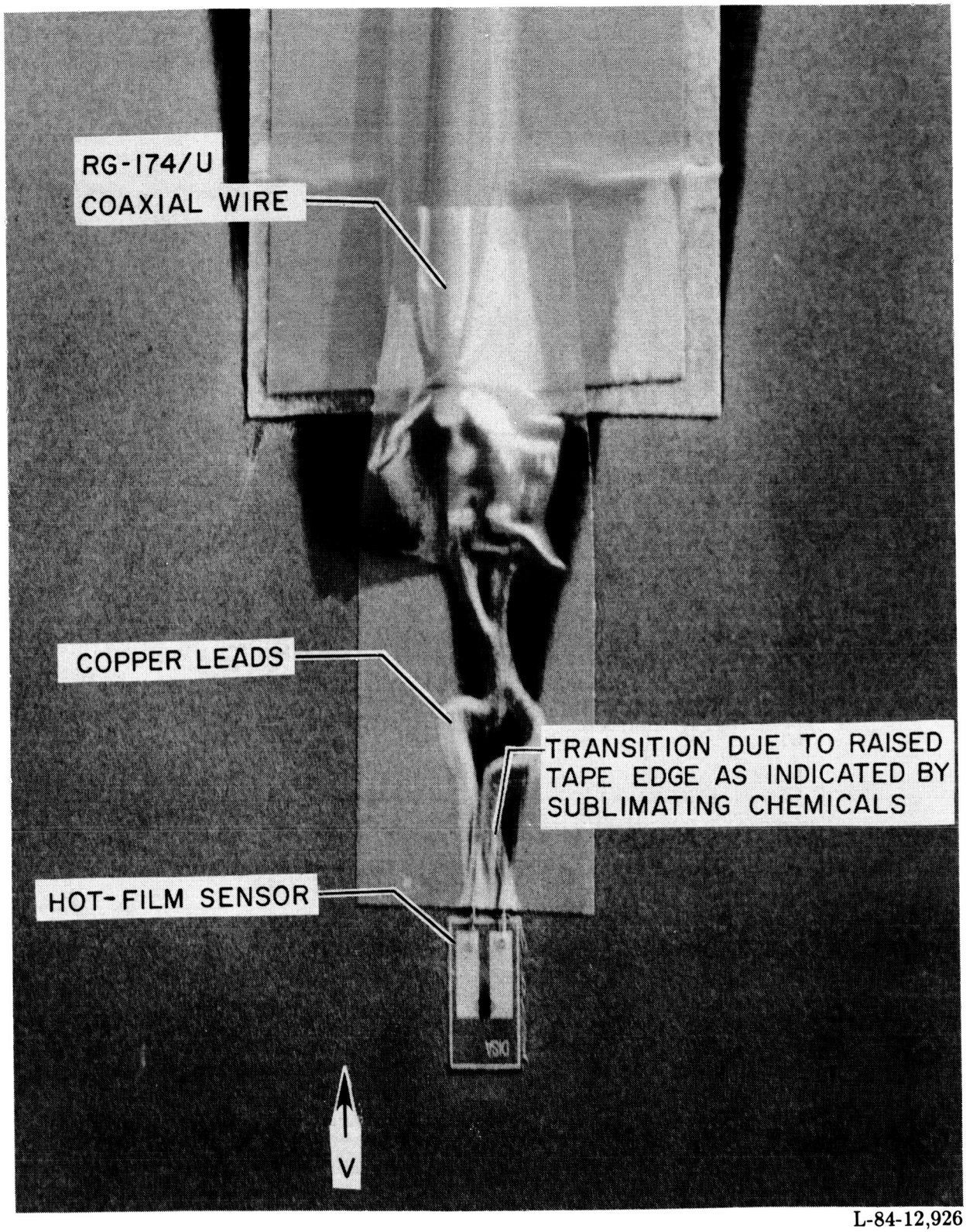

L-84-12,926

Figure 6. Hot-film sensor as mounted on Beechcraft T-34C glove. Tested at $R' = 1.74 \times 10^{-6}$; sensor located at $x/c = 0.20$; Sensor height = 0.004 in.

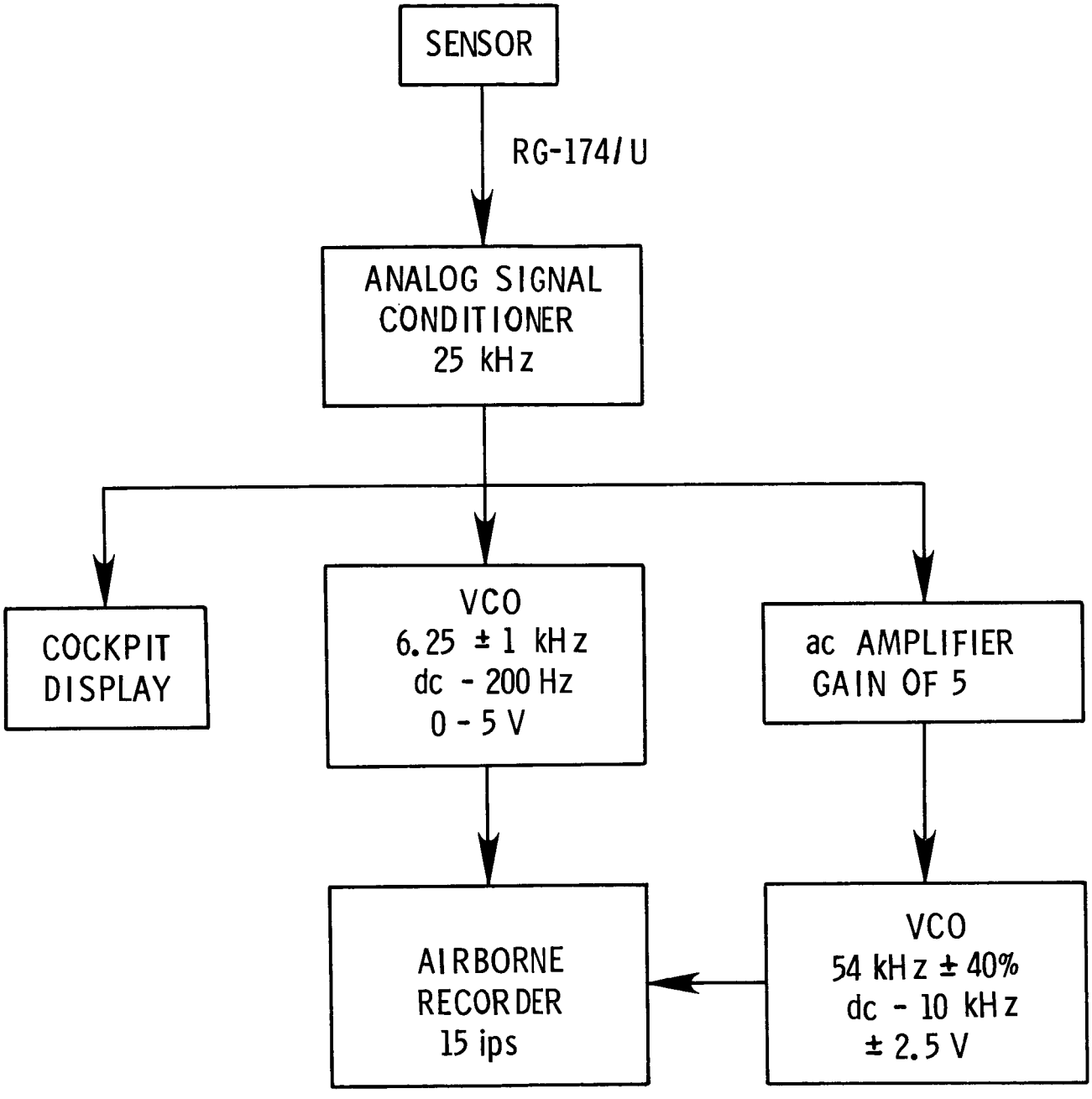

Figure 7. Block diagram of complete flight instrumentation package for hot-film anemometers. (ac amplifier blocks dc component but passes a signal of 0.3 Hz and above.)

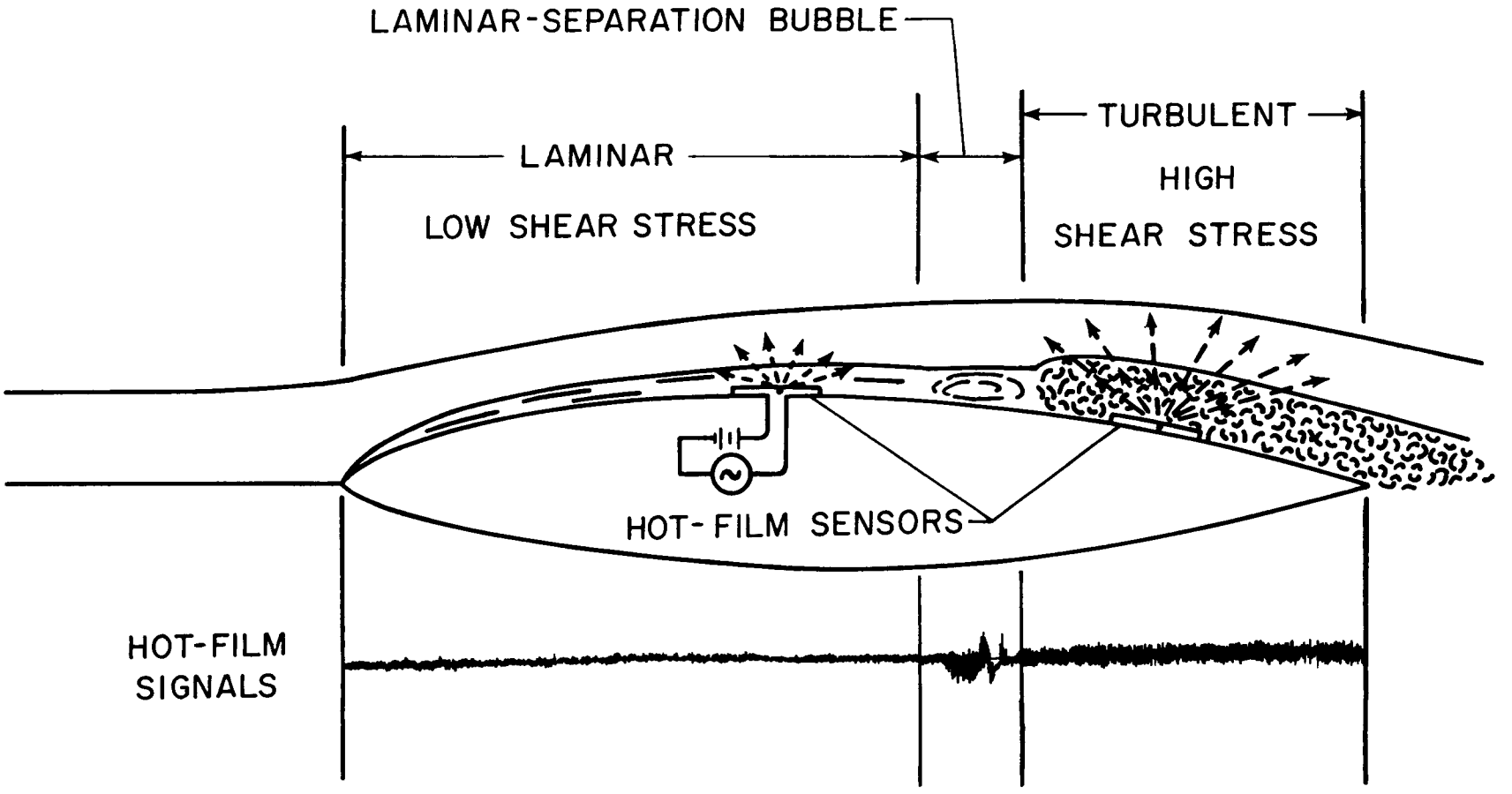

Figure 8. Visual description of how hot-film sensors indicate boundary-layer transition.

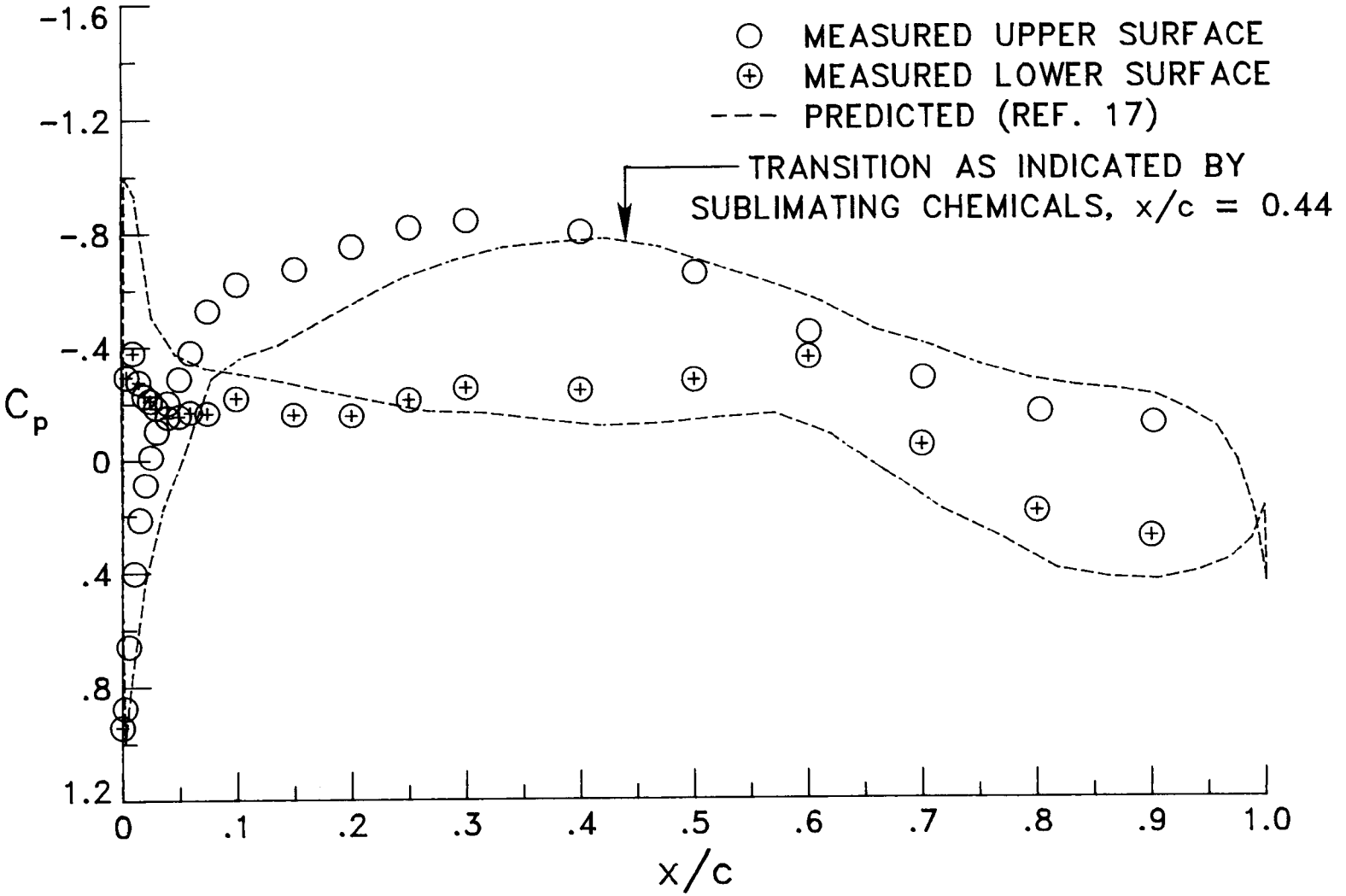

(a) $c_l = 0.35$; $R = 12.6 \times 10^6$; $V_i = 178$ knots; $M = 0.27$.

Figure 9. Beechcraft T-34C NLF glove measured and predicted pressure distributions.

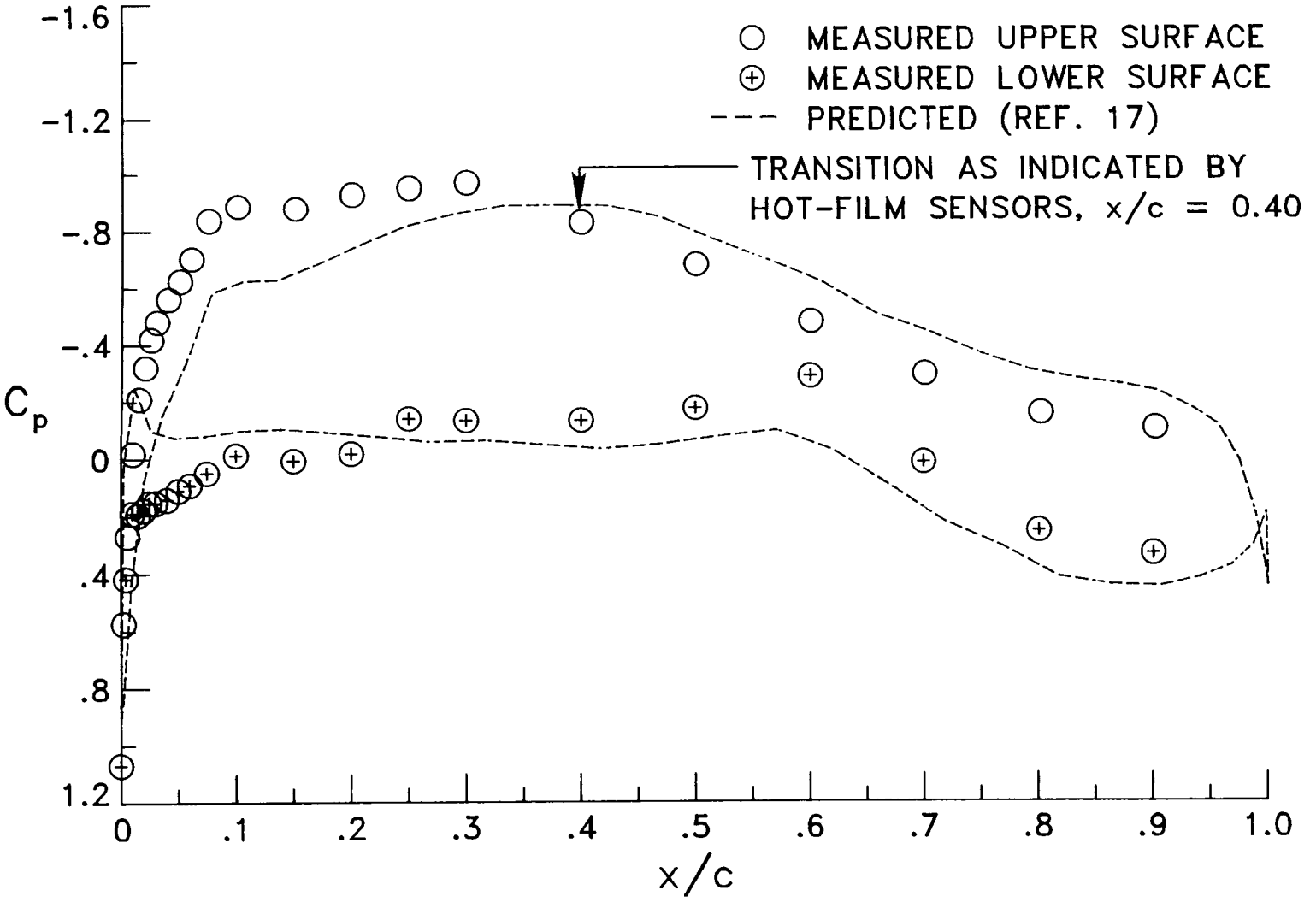

(b) $c_l = 0.54$; $R = 8.6 \times 10^6$; $V_i = 146$ knots; $M = 0.22$.

Figure 9. Continued.

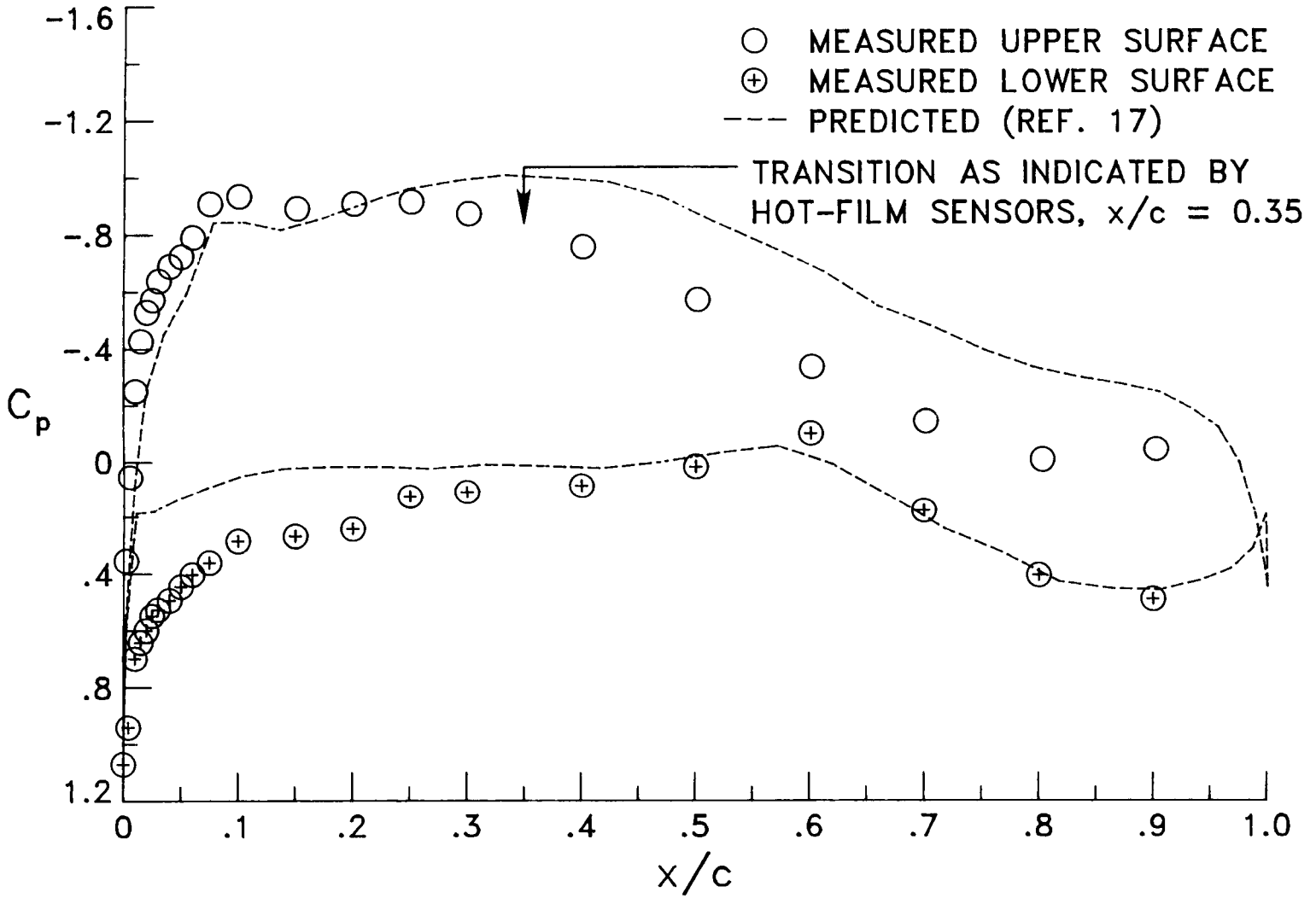

(c) $c_l = 0.69$; $R = 7.6 \times 10^6$; $V_i = 131$ knots; $M = 0.19$.

Figure 9. Concluded.

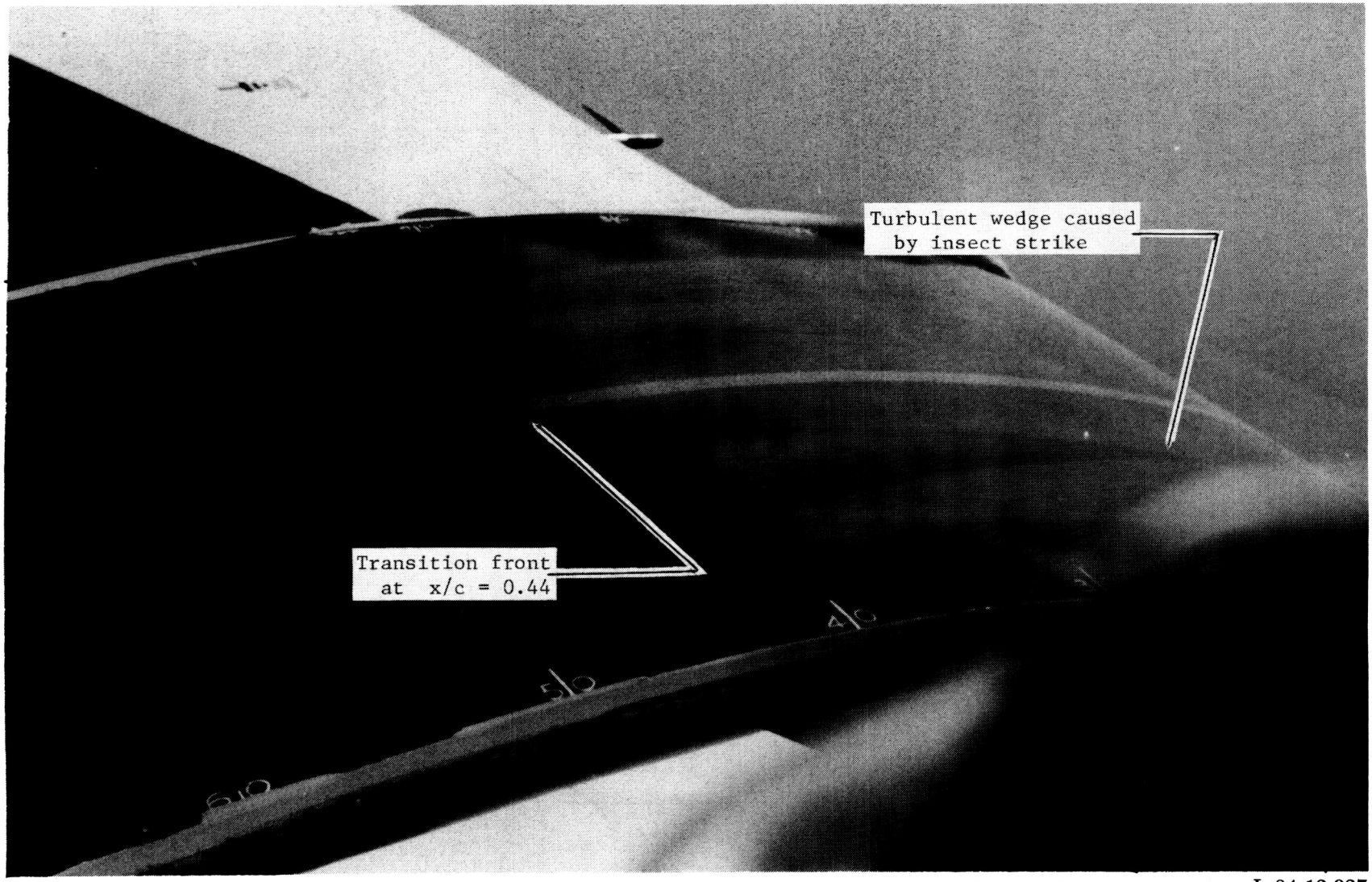

L-84-12,927

Figure 10. Sublimating chemical indication of boundary-layer transition on Beechcraft T-34C NLF glove at $c_l = 0.35$, $R = 12.6 \times 10^6$, $V_i = 178$ knots, and $M = 0.27$.

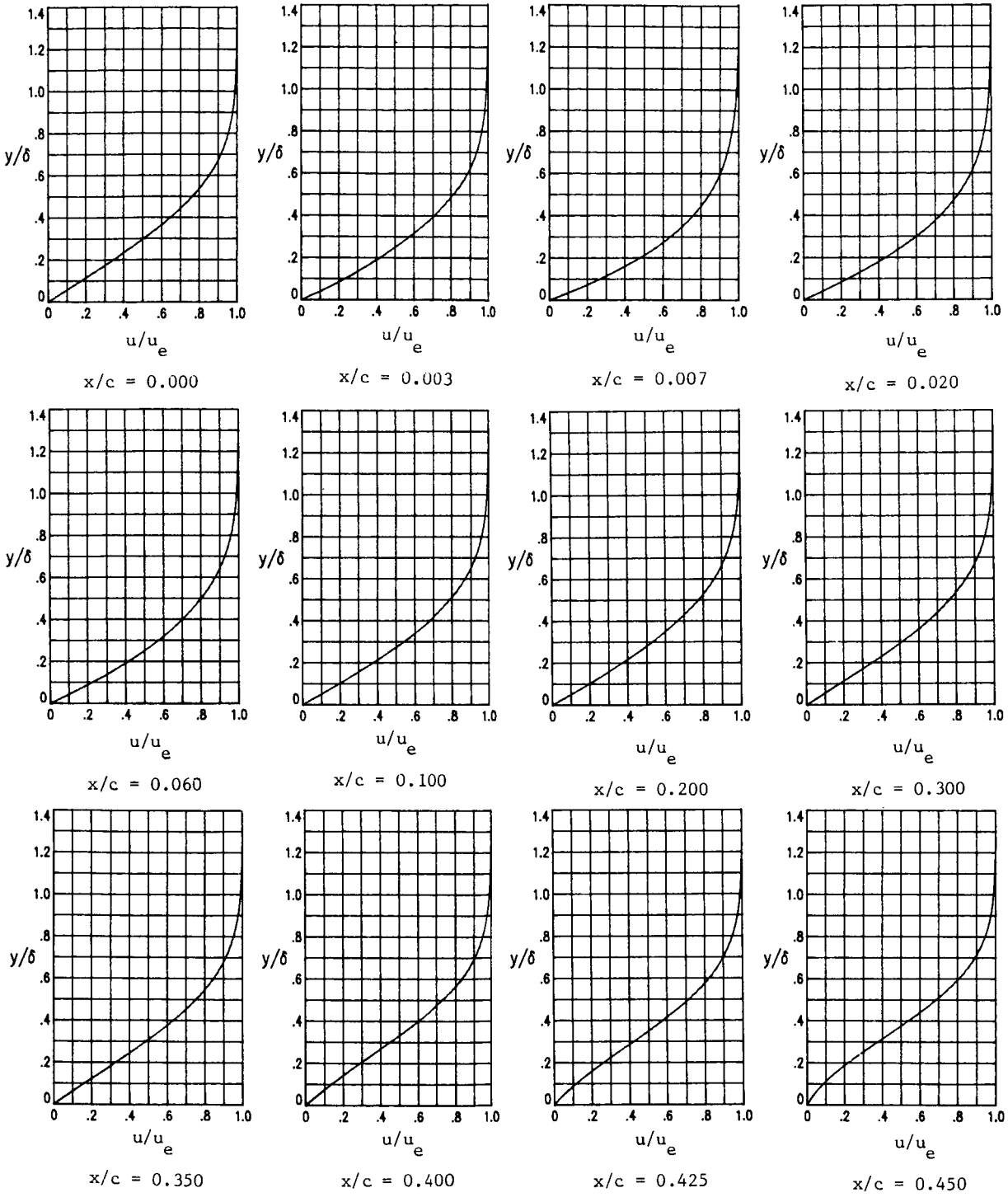

(a) $c_l = 0.35$; $R = 12.6 \times 10^6$; $M = 0.27$.

Figure 11. Beechcraft T-34C NLF glove upper-surface boundary-layer velocity profiles predicted from reference 12. (See parameters in table 4.)

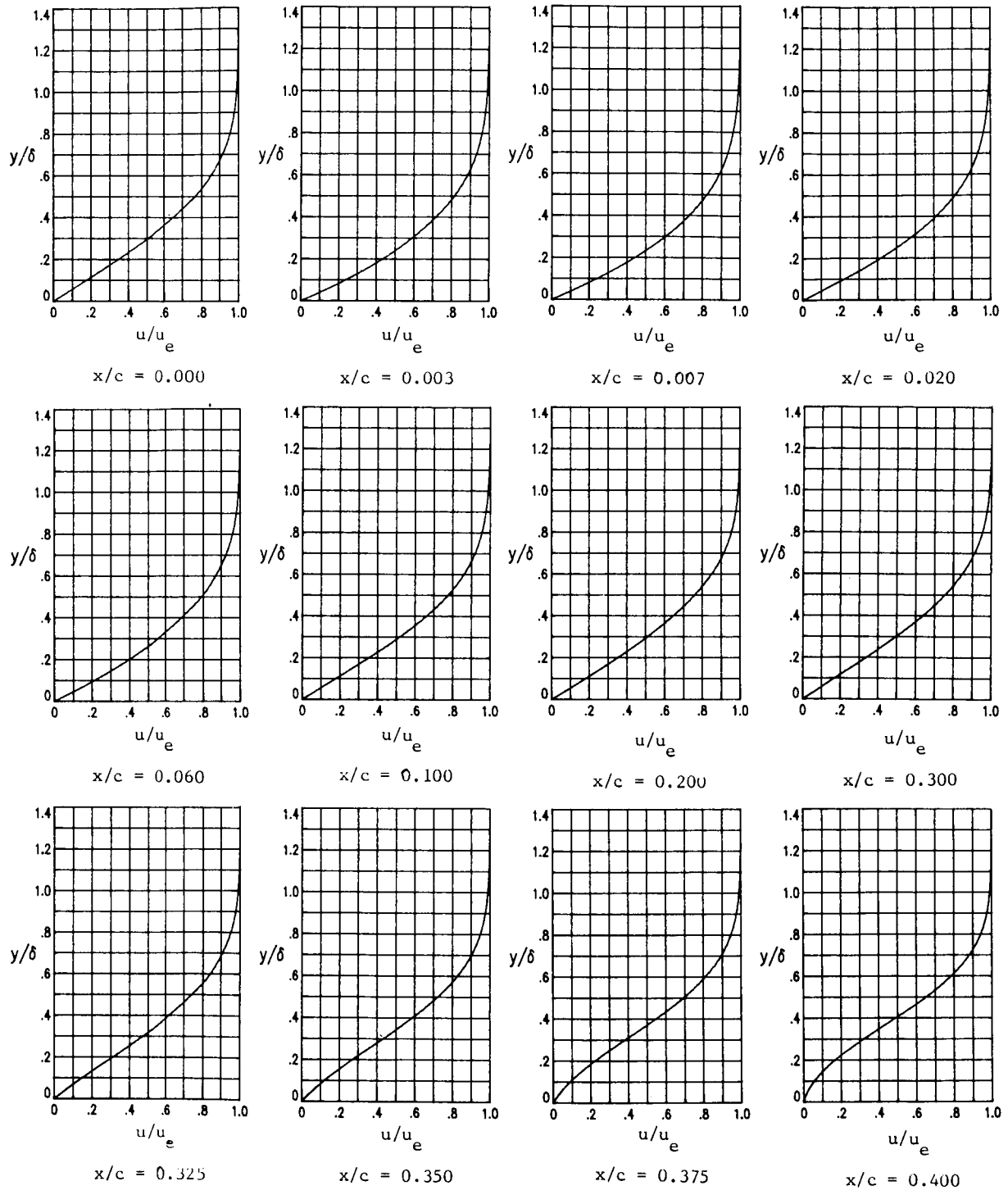

(b) $c_l = 0.54$; $R = 8.6 \times 10^6$; $M = 0.22$.

Figure 11. Concluded.

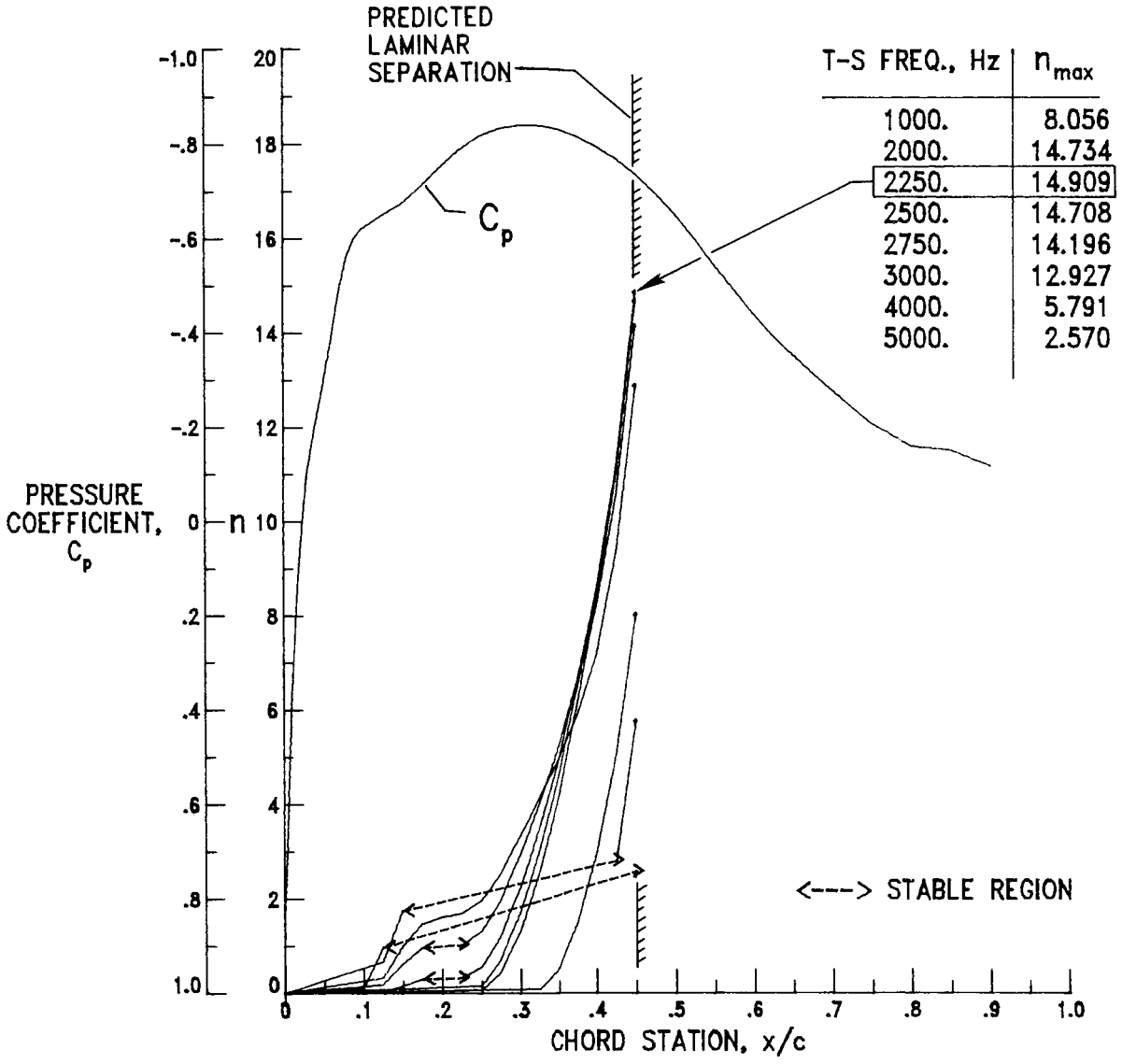

Figure 12. Analysis of maximum amplification ratio of T-S waves for Beechcraft T-34C NLF glove, upper surface. $c_l = 0.35$; $R = 12.6 \times 10^6$; $V_i = 178$ knots; $M = 0.27$.

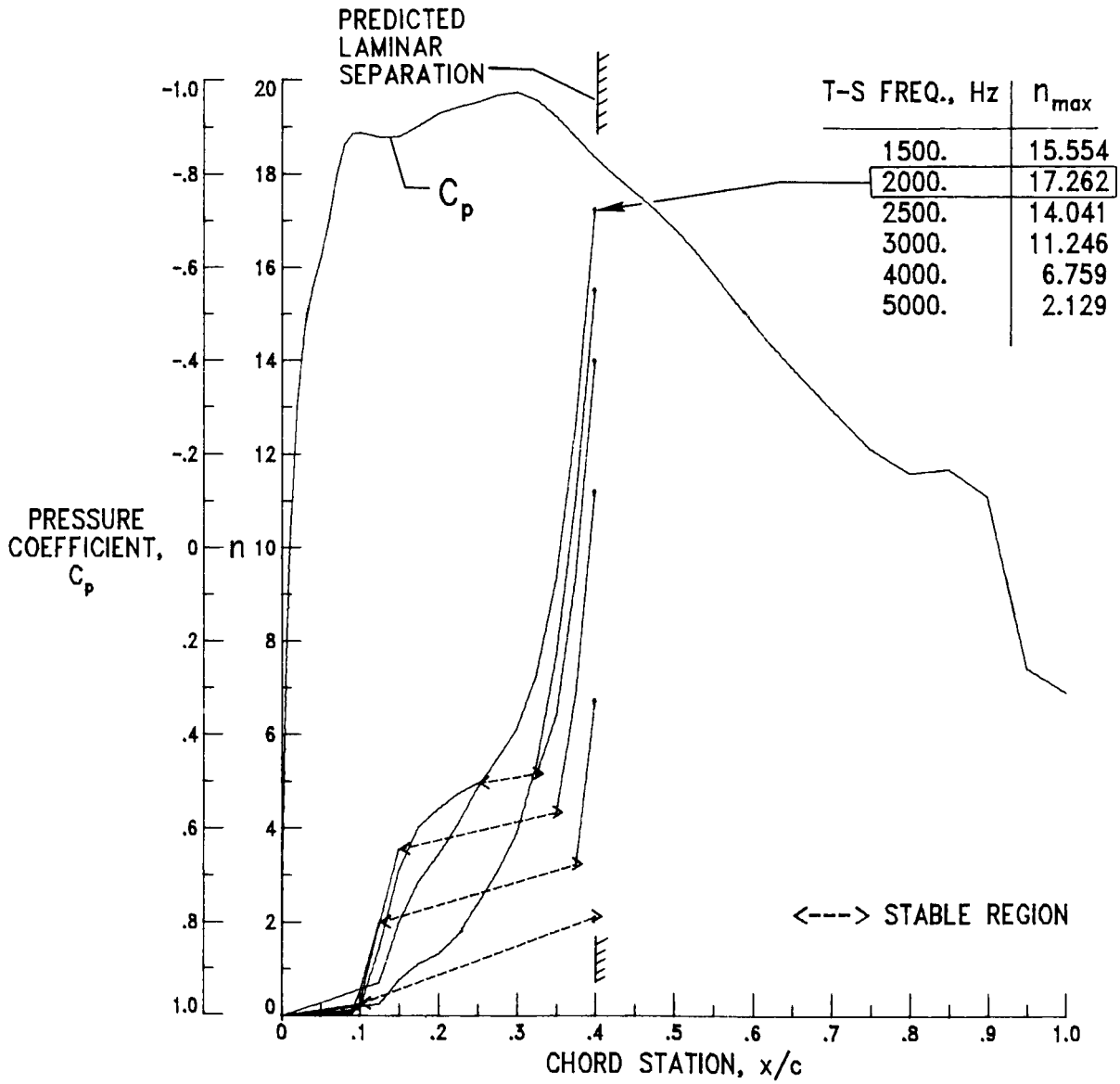

Figure 13. Analysis of maximum amplification ratio of T-S waves for Beechcraft T-34C NLF glove, upper surface. $c_l = 0.54$; $R = 8.6 \times 10^6$; $V_i = 146$ knots; $M = 0.22$.

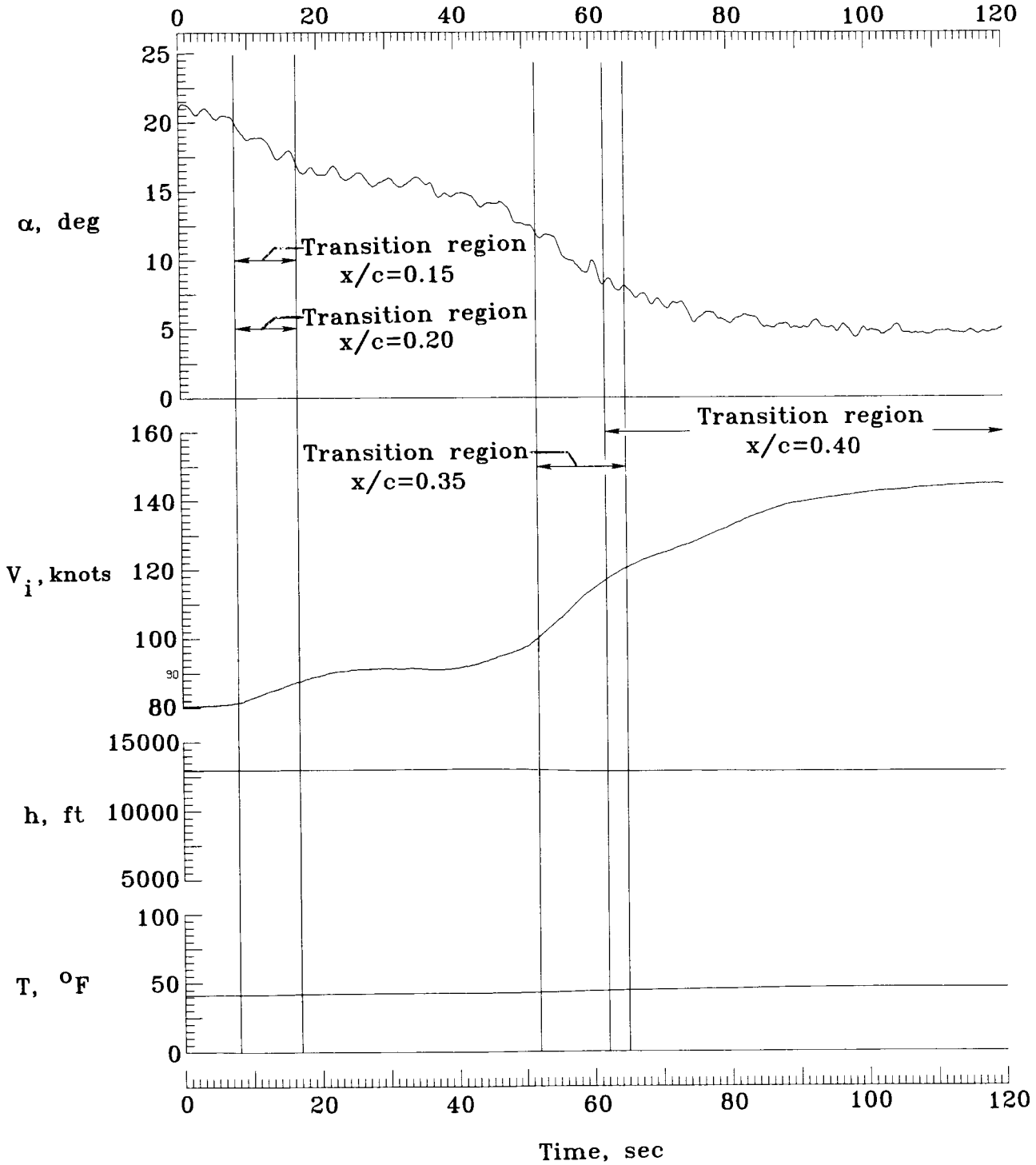

(a) Flight conditions.

Figure 14. Hot-film signals on Beechcraft T-34C NLF glove during accelerated flight. h = 13 000 ft; T = 41°F; V_i = 80 to 145 knots; α = 21° to 5°.

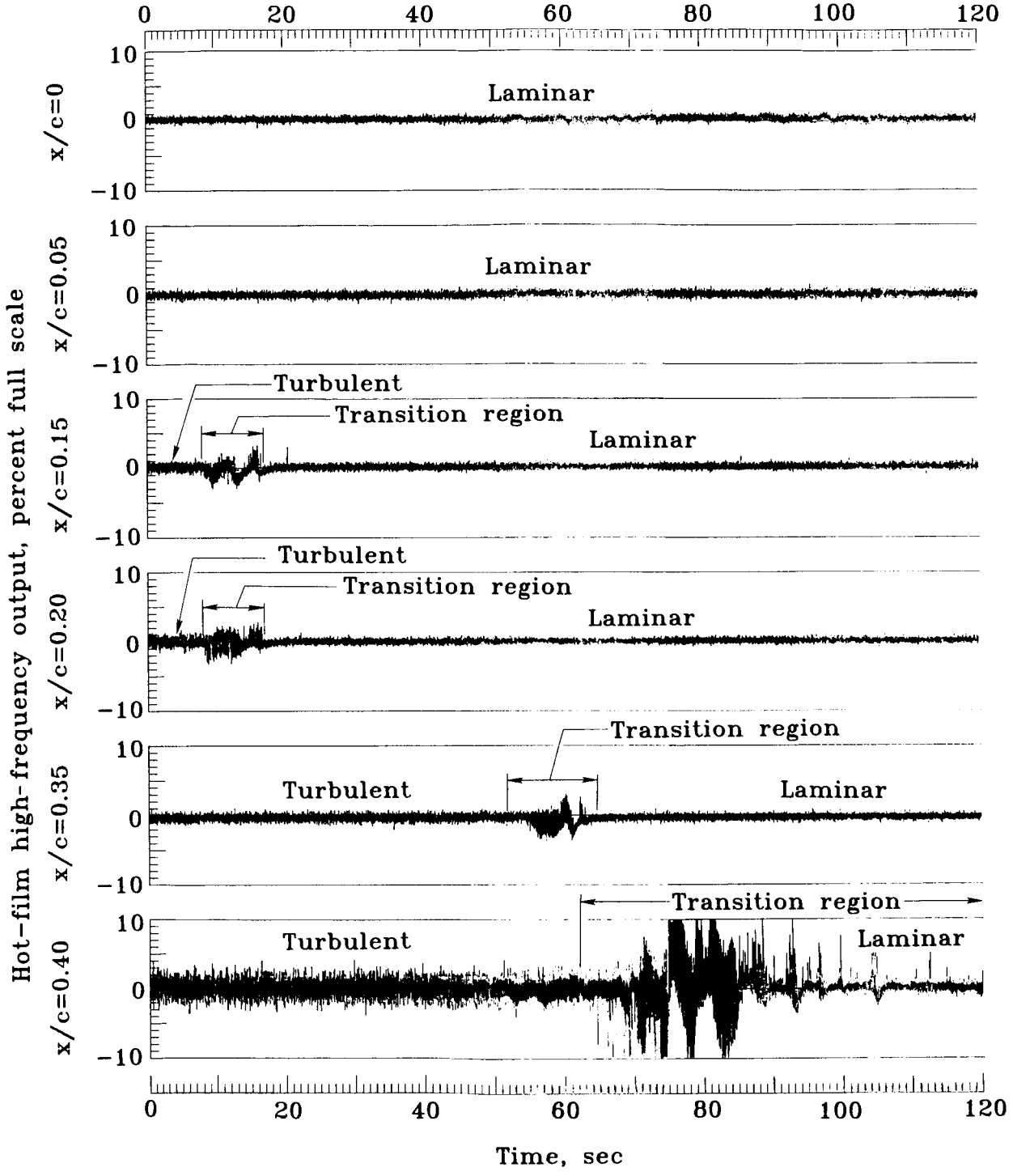

(b) Hot-film ac signals.

Figure 14. Continued.

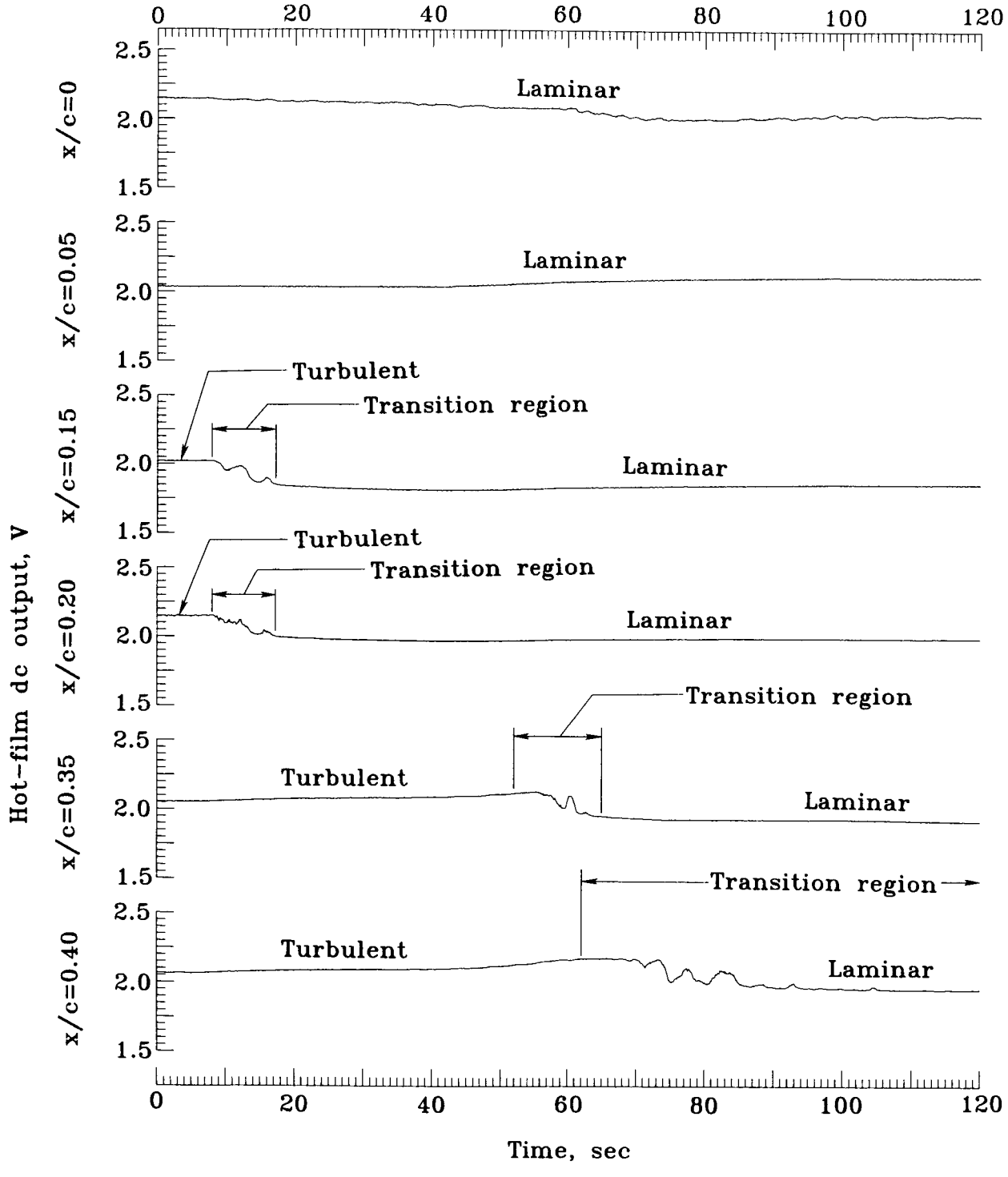

(c) Hot-film steady-state signals.

Figure 14. Concluded.

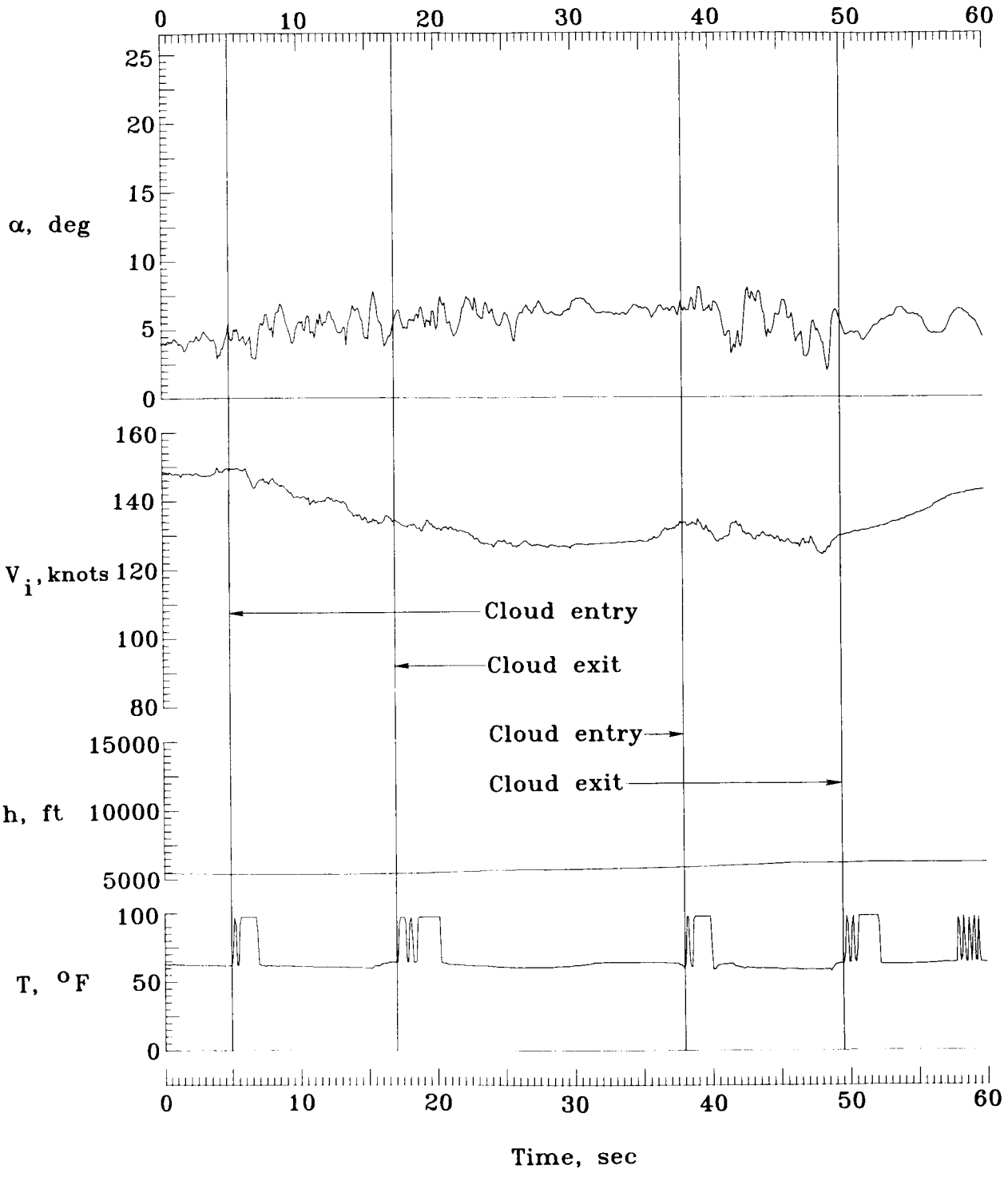

(a) Flight conditions.

Figure 15. Hot-film signals on Beechcraft T-34C NLF glove during flight through clouds with mist deposits. h = 5500 and 6000 ft; T = 62°F; V_i = 150 and 134 knots; $\alpha \approx 5°$.

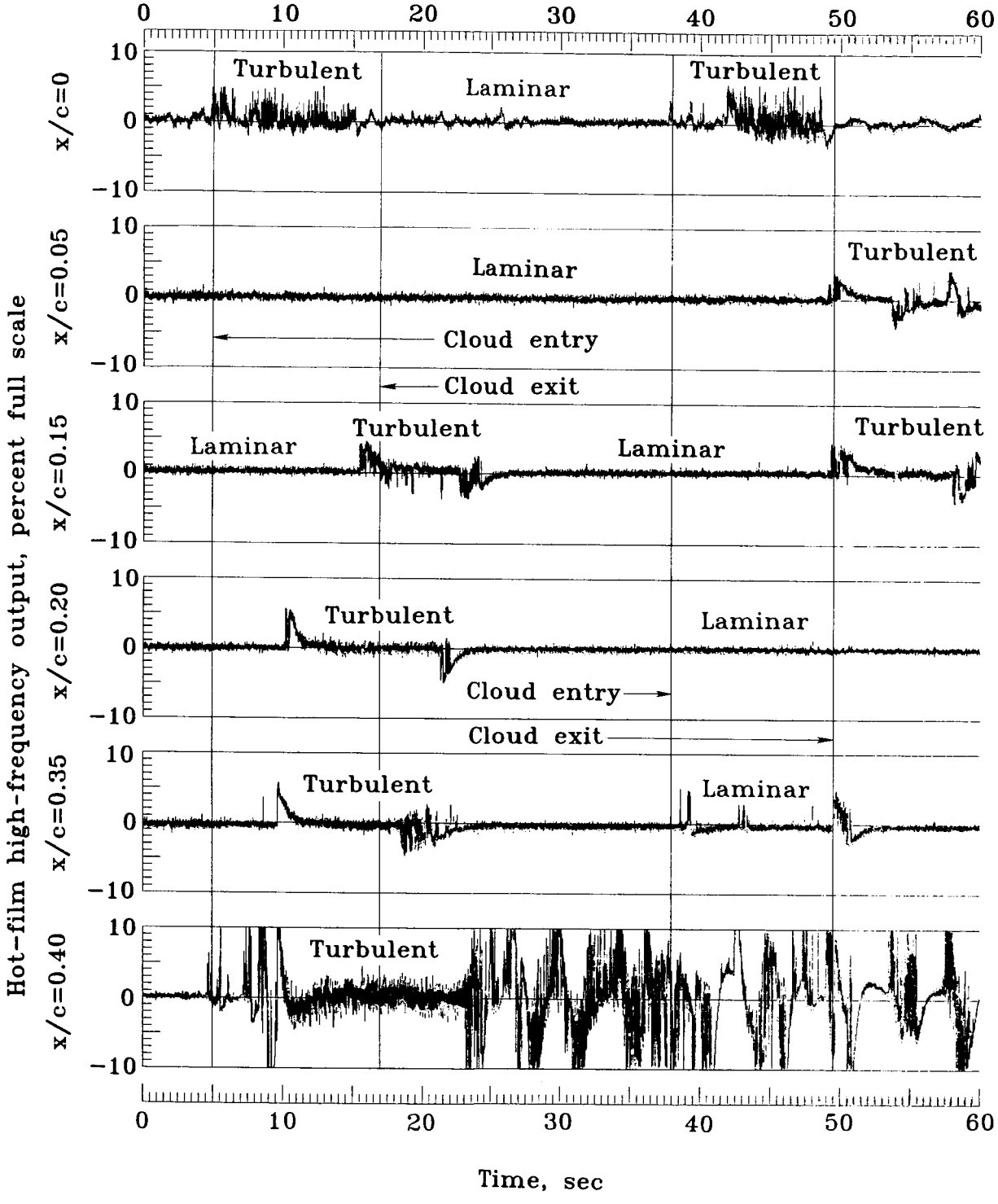

(b) Hot-film ac signals.

Figure 15. Continued.

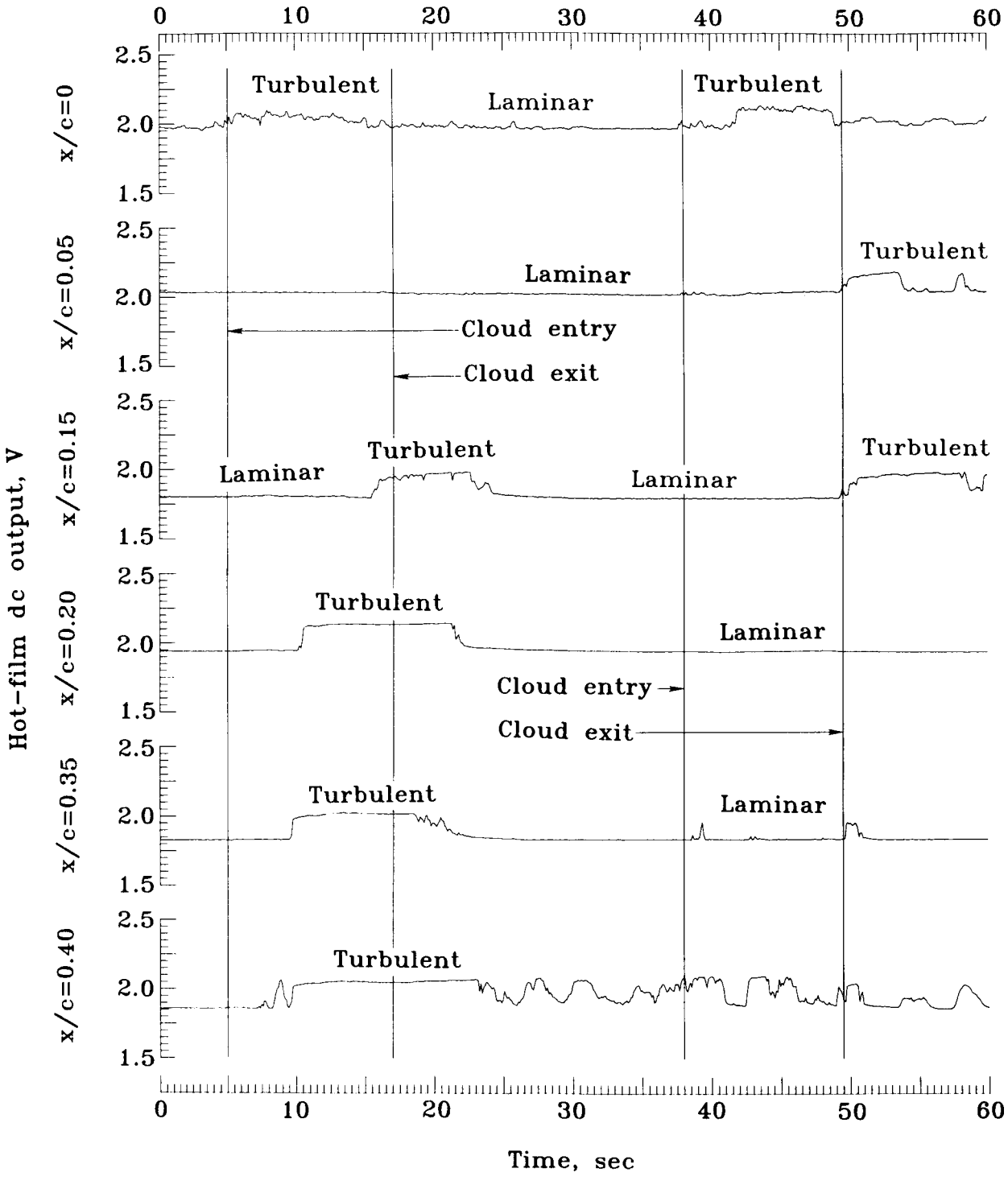

(c) Hot-film steady-state signals.

Figure 15. Concluded.

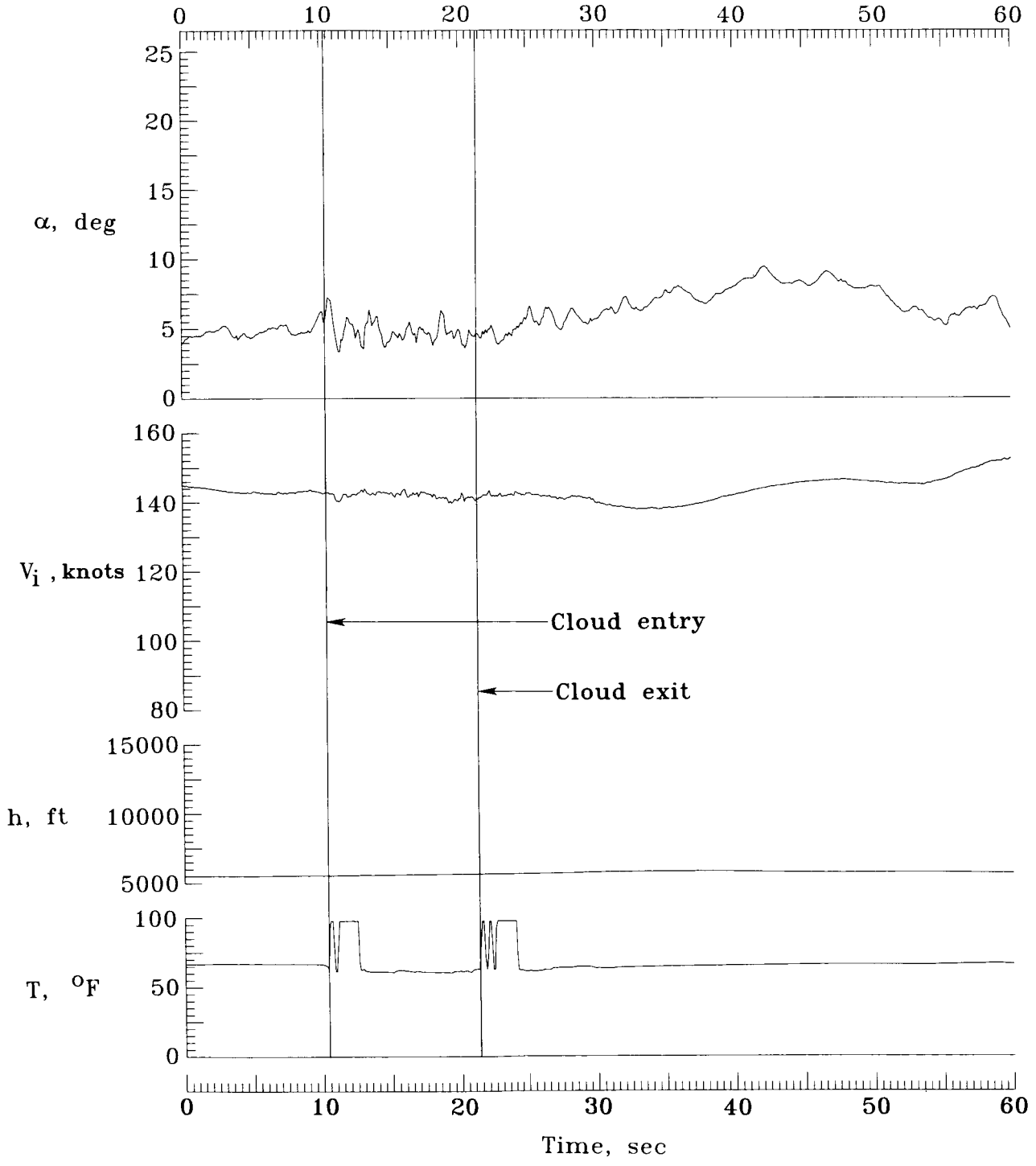

(a) Flight conditions.

Figure 16. Hot-film signals on Beechcraft T-34C NLF glove during flight through clouds with no mist deposits. $h = 5500$ ft; $T = 65°$F; $V_i = 143$ knots; $\alpha \approx 5°$.

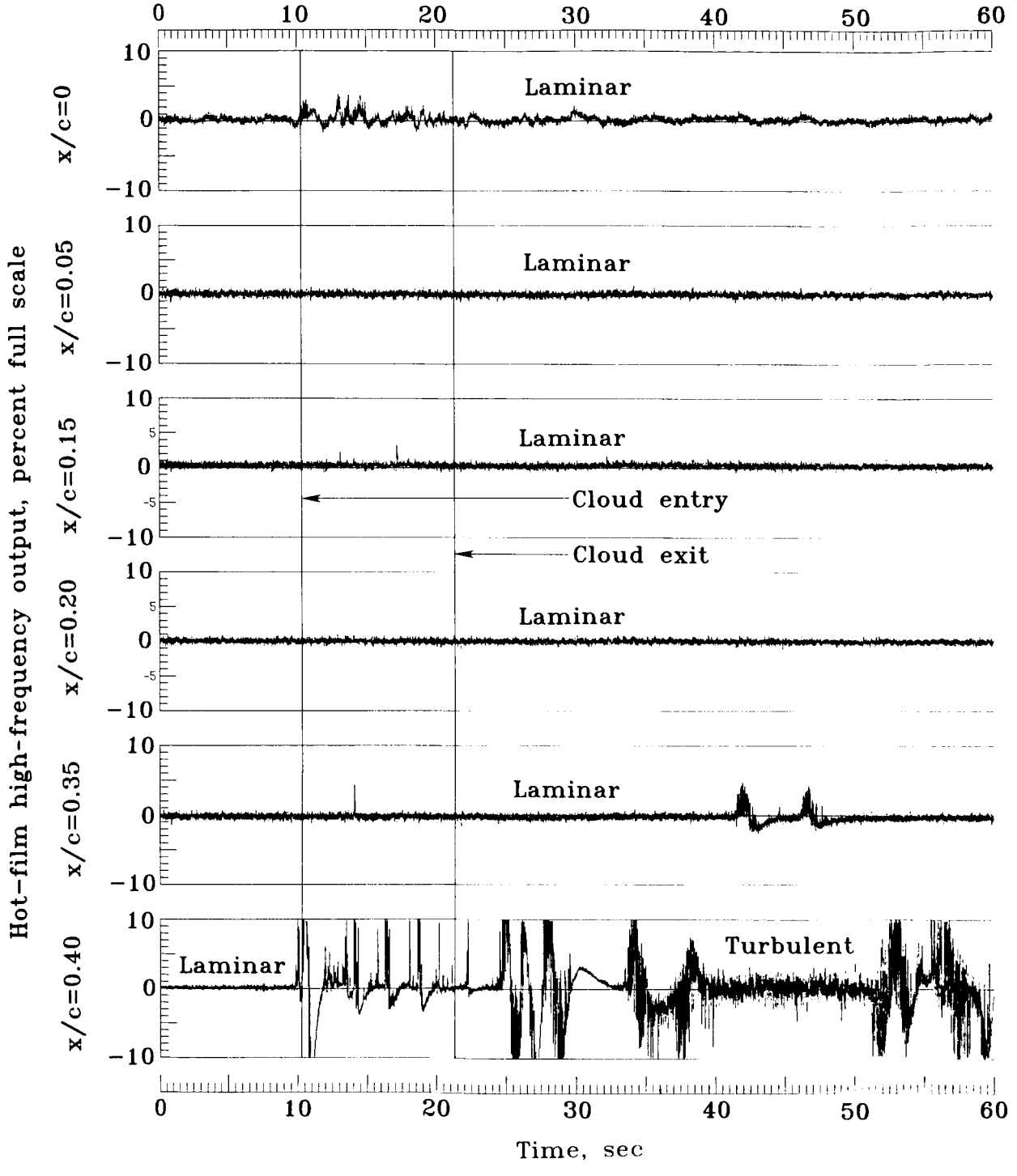

(b) Hot-film ac signals.

Figure 16. Continued.

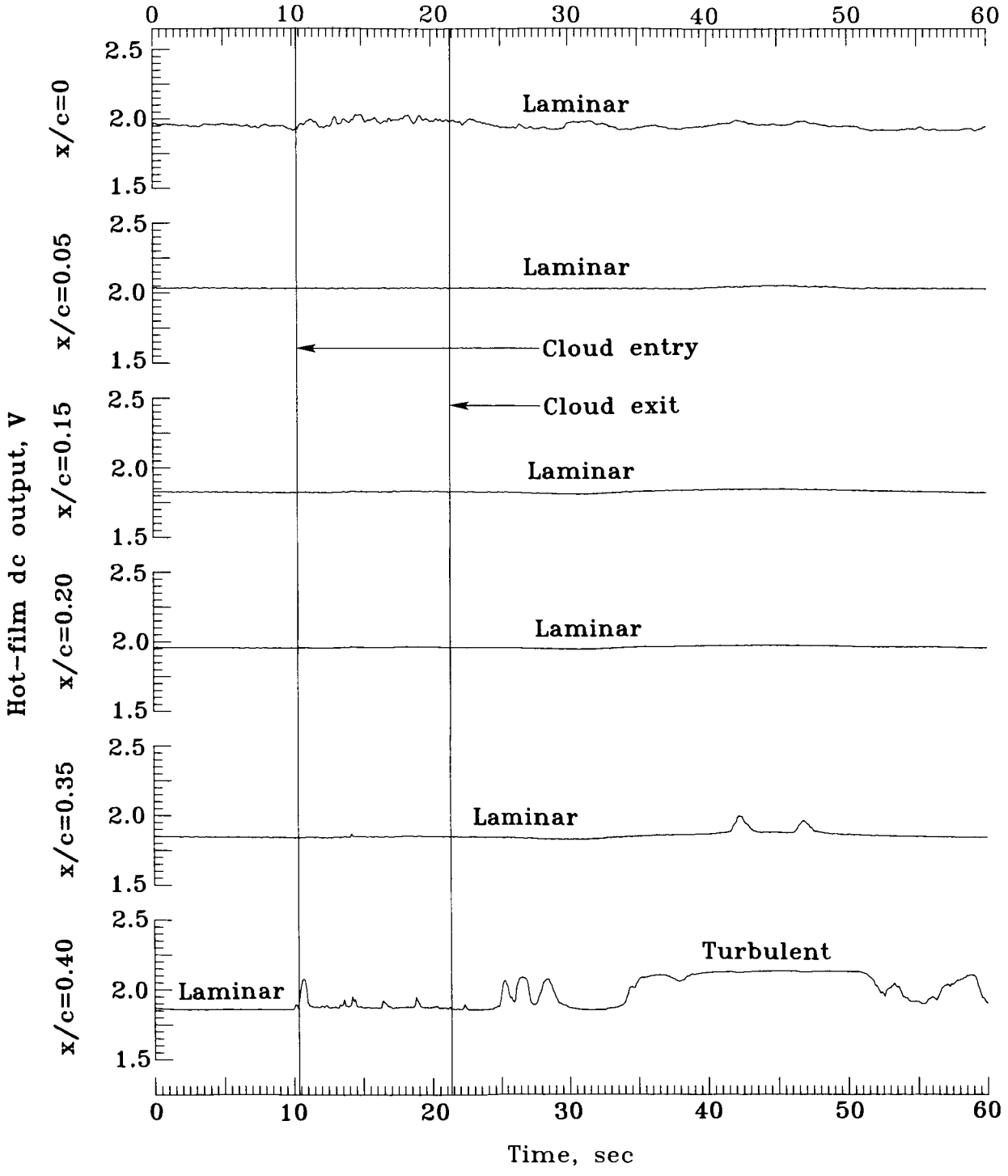

(c) Hot-film steady-state signals.

Figure 16. Concluded.

1. Report No. NASA TP-2417	2. Government Accession No.	3. Recipient's Catalog No.
4. Title and Subtitle Flight-Measured Laminar Boundary-Layer Transition Phenomena Including Stability Theory Analysis		5. Report Date April 1985
		6. Performing Organization Code 505-45-43-02
7. Author(s) Clifford J. Obara and Bruce J. Holmes		8. Performing Organization Report No. L-15804
9. Performing Organization Name and Address NASA Langley Research Center Hampton, VA 23665		10. Work Unit No.
		11. Contract or Grant No.
12. Sponsoring Agency Name and Address National Aeronautics and Space Administration Washington, DC 20546		13. Type of Report and Period Covered Technical Paper
		14. Sponsoring Agency Code

15. Supplementary Notes
Clifford J. Obara: Kentron, International, Inc., Hampton, Virginia.
Bruce J. Holmes: Langley Research Center, Hampton, Virginia.

16. Abstract
Flight experiments were conducted on a single-engine turboprop aircraft fitted with a 92-in-chord, 3-ft-span natural laminar flow glove at Reynolds numbers from 4×10^6 to 13×10^6 and at glove section lift coefficients from 0.15 to 1.10. The boundary-layer transition measurement methods used included sublimating chemicals and surface hot-film sensors. Transition occurred downstream of the minimum pressure point. Hot-film sensors provided a well-defined indication of laminar, laminar-separation, transitional, and turbulent boundary layers. Theoretical calculations of the boundary-layer parameters provided close agreement between the predicted laminar-separation point and the measured transition location. Tollmien-Schlichting (T-S) wave growth n-factors between 15 and 17 were calculated at the predicted point of laminar separation. These results suggest that for many practical airplane cruise conditions, laminar separation (as opposed to T-S instability) is the major cause of transition in predominantly two-dimensional flows.

17. Key Words (Suggested by Authors(s))
Laminar flow
Natural laminar flow
Boundary-layer transition
Flight experiments
Boundary-layer stability

18. Distribution Statement
Unclassified—Unlimited

Subject Category 02

19. Security Classif.(of this report)	20. Security Classif.(of this page)	21. No. of Pages	22. Price
Unclassified	Unclassified	38	A03

For sale by the National Technical Information Service, Springfield, Virginia 22161

NASA-Langley, 1985